# D 1 Atomic and Magnetic Structures in Crystalline Materials: Neutron and X-ray Scattering

Thomas Brückel

Institut für Festkörperforschung

Forschungszentrum Jülich GmbH

## Contents

# 1 Introduction

Our present understanding of the properties and phenomena of condensed matter science is based on atomic theories. The first question we pose when studying any condensed matter system is the question concerning the internal structure: what are the relevant building blocks (atoms, molecules, colloidal particles, ...) and how are they arranged? The second question concerns the microscopic dynamics: how do these building blocks move and what are their internal degrees of freedom? For magnetic systems, in addition we need to know the arrangement of the microscopic magnetic moments due to spin and orbital angular momentum and their excitation spectra. In principle, the macroscopic response and transport properties such as specific heat, thermal conductivity, elasticity, viscosity, susceptibility, magnetization etc., which are the quantities of interest for applications, result from the microscopic structure and dynamics. To determine these macroscopic properties from the microscopic information provided by experiment represents a huge challenge to condensed matter theory as we are dealing with an extreme many body problem with typically $10^{23}$ particles involved. It is a true masterly achievement of mankind that for many solid state systems, such microscopic theories could be developed based on quantum mechanics and statistical physics.

For the development of modern condensed matter research, the availability of probes to study the structure and dynamics on a microscopic level is therefore essential. Modern scattering techniques can provide all the required information. Radiation, which has rather weak interaction with a sample under investigation provides a non-invasive, non-destructive probe for the microscopic structure and dynamics. This has been shown for the first time by W. Friedrich, P. Knipping and M. von Laue in 1912, when interference of x-ray radiation from a single crystal was observed. Max von Laue received the Nobel prize for the interpretation of these observations. One cannot overestimate this discovery: it was the first proof that atoms are the elementary building blocks of condensed matter and that they are arranged in a periodic manner within a crystal. The overwhelming part of our present-day knowledge of the atomic structure of condensed matter is based on x-ray structure investigations. Of course the method has developed rapidly since 1912. With the advent of modern synchrotron x-ray sources, the source brilliance has since then increased by 18 orders of magnitude. Currently x-ray Free Electron Lasers, e. g. the XFEL project (http://xfel.desy.de/), are proposed which will increase this brilliance by another 10 orders of magnitude. Nowadays the structure of highly complex biological macromolecules can be determined with atomic resolution such as the crystal structure of the ribosome. Extremely weak phenomena such as magnetic x-ray scattering can be exploited successfully at modern synchrotron radiation sources. Besides x-ray scattering, light scattering is an important tool in soft condensed matter research, where one is interested in the dynamics on larger lengths scales, such as of colloidal particles in solution. Finally, intense neutron beams have properties, which make them an excellent probe for condensed matter investigations. Neutron scattering is a unique tool to solve magnetic structures and determine magnetic excitations and fluctuations. In soft matter and life science, neutrons excel due to the possibility to apply contrast variation techniques by selective deuteration of molecules or molecular subunits. Neutrons give access to practically all lengths scales relevant in condensed matter investigations from the atomic level up to about 1000 nm and are particularly well suited for the investigations of the movement of atoms and molecules. As with x-rays, the experimental techniques are in rapid evolution, mainly due to the advent of new neutron optical devices, and the new spallation sources such as the American Spallation Neutron Source SNS (http://www.sns.gov/) or the proposed European Spallation Source ESS (http://neutron.neutron-eu.net/n_ess) will increase the capabilities of neutron investigations in condensed matter science drastically in the years to come.

In the following we give an elementary introduction into scattering theory in general and show some applications in structure determination for crystalline materials. More details can be found in [1-4].

This lecture is organised as follows: first we give a very basic introduction into elementary scattering theory for elastic scattering, followed by a more rigorous derivation in the framework of the Born series. We will introduce the concepts of coherence and pair correlation functions. Then we will discuss, which probes are most relevant for condensed matter investigations and derive the cross sections for the main interaction processes with matter. Finally we will give some topical examples for structural studies using neutrons and x-rays.

I have to emphasise that a lecture on scattering for all the different probes and for the static and dynamic cases is a subject for a full semester university course. With the limited space available it is impossible to deduce the results cited in a strict manner. I will use simple hand waving arguments to motivate the form of the equations presented and refer to the literature [1-4] for the detailed derivation.

We will frequently make use of the particle-wave dualism of quantum mechanics, which tells us that the radiation used in the scattering process can be described in a wave picture, whenever we are interested in interference phenomena and in a particle picture when the interaction with matter is relevant, e. g. for the detection process.

# 2 Elementary Scattering Theory: Elastic Scattering

## 2.1 Scattering Geometry and Scattering Cross Section

Throughout this lecture we assume that the atoms within our sample are rigidly fixed on equilibrium positions in space. Therefore we only look at those processes, in which the recoil is being transferred to the sample as a whole so that the energy change for the radiation is negligible and the scattering process appears to be elastic. In subsequent lectures, this restriction will be dropped and so-called inelastic scattering processes will be discussed due to excitations or internal fluctuations in the sample, which give rise to an energy change of the radiation during the scattering process.

A sketch of the scattering experiment is shown in Figure 1.

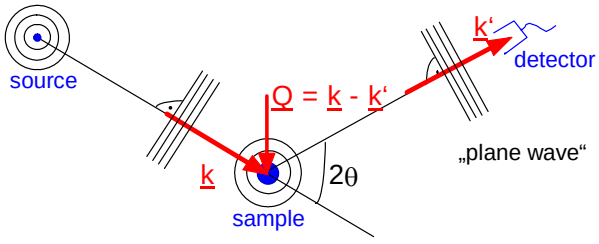


**Figure 1** *A sketch of the scattering process in the Fraunhofer approximation in which it is assumed that plane waves are incident on sample and detector due to the fact that the distance source-sample and sample-detector, respectively, is significantly larger than the size of the sample.*

Here we assume the so-called *Fraunhofer approximation*, where the size of the sample has to be much smaller than the distance between sample and source and the distance between sample and detector, respectively. This assumption holds in all cases discussed in this lecture. In addition we assume that the source emits radiation of one given energy, i. e. so-called *monochromatic* radiation. Then the wave field incident on the sample can be considered as a plane wave, which is completely described by a wave vector $\underline{k}$. The same holds for the wave incident on the detector, which can be described by a vector $\underline{k}'$. In the case of elastic scattering (diffraction) we have

$$k = |\underline{k}| = |\underline{k}'| = k' = \frac{2\pi}{\lambda} \tag{1}$$

Let us define the so-called *scattering vector* by

$$\underline{Q} = \underline{k} - \underline{k}' \tag{2}$$

$\hbar\underline{Q}$ represents the momentum transfer during scattering, since according to de Broglie, the momentum of the particle corresponding to the wave with wave vector $\underline{k}$ is given by $\underline{p}=\hbar\underline{k}$. The magnitude of the scattering vector can be calculated from wavelength $\lambda$ and scattering angle $2\theta$ as follows

$$Q = |\underline{Q}| = \sqrt{k^2 + k'^2 - 2kk'\cos 2\theta} \Rightarrow Q = \frac{4\pi}{\lambda}\sin\theta \tag{3}$$

A scattering experiment comprises the measurement of the intensity distribution as a function of the scattering vector. The scattered intensity is proportional to the so-called *cross section*, where the proportionality factors arise from the detailed geometry of the experiment. For a definition of the scattering cross section, we refer to Figure 2.

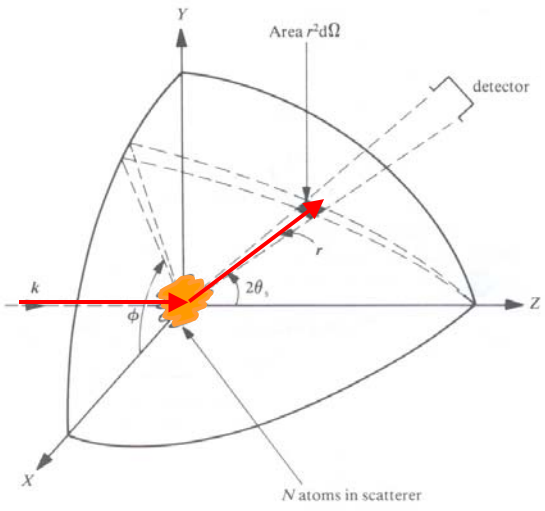


**Figure 2** *Geometry used for the definition of the scattering cross section.*

If n' particles are scattered per second into the solid angle dΩ seen by the detector under the scattering angle 2θ and into the energy interval between E' and E' + dE', then we can define the so-called *double differential cross section* by:

$$\frac{d^2\sigma}{d\Omega dE'} = \frac{n'}{j d\Omega dE'} \tag{4}$$

Here j refers to the incident beam flux in terms of particles per area and time. If we are not interested in the change of the energy of our radiation during the scattering process, or if our detector is not able to resolve this energy change, then we will describe the angular dependence by the so-called *differential cross section:*

$$\frac{\mathrm{d}\sigma}{\mathrm{d}\Omega} = \int_0^\infty \frac{\mathrm{d}^2\sigma}{\mathrm{d}\Omega \mathrm{dE}'} \mathrm{dE}' \tag{5}$$

Finally the so-called *total scattering cross section* gives us a measure for the total scattering probability independent of changes in energy and scattering angle:

$$\sigma = \int_0^{4\pi} \frac{d\sigma}{d\Omega} d\Omega \tag{6}$$

Our task therefore is to determine the arrangement of the atoms in the sample from the knowledge of the scattering cross section $\mathrm{d}\sigma/\mathrm{d}\Omega$. The relationship between scattered intensity and the structure of the sample is particularly simple in the so-called *Born approximation*, which is often also referred to as *kinematic scattering approximation*. In this case, refraction of the beam entering and leaving the sample, multiple scattering events and the extinction of the primary beam due to scattering within the sample are being neglected. Following Figure 3, the phase difference between a wave scattered at the origin of the coordinate system and at position $\underline{r}$ is given by

$$\Delta\Phi = 2\pi \cdot \frac{\left(\overline{AB} - \overline{CD}\right)}{\lambda} = \underline{k}' \cdot \underline{r} - \underline{k} \cdot \underline{r} = \underline{Q} \cdot \underline{r} \tag{7}$$

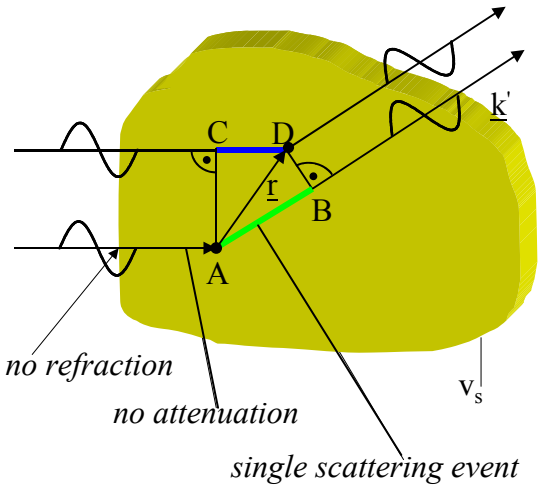


**Figure 3** *A sketch illustrating the phase difference between a beam scattered at the origin of the coordinate system and a beam scattered at the position* $\underline{r}$.

The scattered amplitude at the position $\underline{r}$ is proportional to the scattering power density, or simply scattering density $\rho_s(\underline{r})$. $\rho_s$ depends on the type of radiation used and its interaction with the sample. In fact, $\rho_s$ is directly proportional to the interaction potential, as will be shown in the next chapter. Assuming a laterally coherent beam, the total scattering amplitude is given by a coherent superposition of the scattering from all points within the sample, i. e. by the integral

$$A = A_0 \cdot \int_{V_S} \rho_S(\underline{r}) \cdot e^{i\underline{Q}\cdot\underline{r}} d^3r \qquad (8)$$

Here $A_0$ denotes the amplitude of the incident wave field. (8) demonstrates that the scattered amplitude is connected with the scattering power density $\rho_s(\underline{r})$ by a simple Fourier transform. A knowledge of the scattering amplitude for all scattering vectors $\underline{Q}$ allows us to determine via a Fourier transform the scattering power density uniquely. This is the complete information on the sample, which can be obtained by the scattering experiment. Unfortunately nature is not so simple. On one hand, there is the more technical problem that one is unable to determine the scattering cross section for <u>all</u> values of momentum transfer $\hbar\underline{Q}$. The more fundamental problem, however, is given by the fact that normally the amplitude of the scattered wave is not measurable. Instead only the scattered intensity

$$I \sim |A|^2 \qquad (9)$$

can be determined. Therefore the phase information is lost and the simple reconstruction of the scattering density via a Fourier transform is no longer possible. This is the so-called *phase problem* of scattering. There are ways to overcome the phase problem, i.e. by the use of reference waves. Then the scattering density becomes directly accessible. The question, which

information we can obtain from a scattering experiment despite the phase problem will be addressed below.

Which wavelength do we have to choose to obtain the required real space resolution? For information on a length scale L, a phase difference of about $Q \cdot L \approx 2\pi$ has to be achieved. Otherwise according to (7) $\underline{k}'$ and $\underline{k}$ will not differ significantly. According to (3) $Q \approx 2\pi/\lambda$ for typical scattering angles ($2\theta \sim 60°$). Combining these two estimates, we end up with the requirement that the wavelength $\lambda$ has to be in the order of the real space length scale L under investigation. To give an example: with the wavelength in the order of 0.1 nm, atomic resolution can be achieved in a scattering experiment.

## 2.2 Fundamental Scattering Theory: The Born Series

In this chapter, we will give a simple formulation of scattering theory. Our purpose is to derive (8) from fundamental principles. The conditions under which (8) holds and the limitations of kinematical scattering theory will thus become clearer. The derivation will be done for particle beams – in particular neutrons - for which the Schrödinger equation holds. More details can be found in [4].

In quantum mechanics, neutrons are described as particle wave fields through the Schrödinger equation:

$$H\Psi = \left( -\frac{\hbar^2}{2m_n}\Delta + V \right)\Psi = i\hbar\frac{\partial}{\partial t}\Psi \tag{10}$$

$\psi$ is the probability density amplitude, V the interaction potential. In the case of purely elastic scattering E = E', the time dependence can be described by the factor $\exp\left(-i\frac{E}{\hbar}t\right)$. Assuming this time dependence, a wave equation for the spatial part of the probability density amplitude $\psi$ can be derived from (10):

$$\Delta\Psi + k^2\left(\underline{r}\right)\Psi = 0 \tag{11}$$

In (11) we have introduced a spatially varying wave vector with the magnitude square:

$$k^2\left(\underline{r}\right) = \frac{2m_n}{\hbar^2}\left(E - V\left(\underline{r}\right)\right) \tag{12}$$

Solutions of (10) in empty space can be guessed immediately. They are given by plane waves $\Psi = \Psi_0 \exp\left[ i\left( \underline{k} \cdot \underline{r} - \frac{E}{\hbar} t \right) \right]$ with $k^2 = \frac{2m_n}{\hbar^2} E$. The relations between magnitude of the wave vector, wave length and energy of the neutron E can be written in practical units:

$$
\begin{aligned}
k\left[ \text{Å}^{-1} \right] &\approx 0.695 \sqrt{E\left[ meV \right]} \\
\lambda\left[ \text{Å} \right] &\approx 9.045 / \sqrt{E\left[ meV \right]} \\
E\left[ meV \right] &\approx 81.8 / \lambda^2 \left[ \text{Å} \right]
\end{aligned}
\qquad (13)
$$

To give an example, neutrons of wavelength λ = 2.4 Å = 0.24 nm have an energy of 14.2 meV with a magnitude of the neutron wave vector of k = 2.6 Å$^{-1}$.

To obtain solutions of the wave equation (11) in matter, we reformulate the differential equation by explicitly separating the interaction term:

$$\left( \Delta + k^2 \right) \Psi = \frac{2m_n}{\hbar^2} V \cdot \Psi =: \chi \qquad (14)$$

Here $\underline{k}$ denotes the wave vector for propagation in empty space. The advantage of this formulation is that the solutions of the left hand side are already known. They are the plane waves in empty space. Equation (14) is a linear partial differential equation, i. e. the superposition principle holds: the general solution can be obtained as a linear combination of a complete set of solution functions. The coefficients in the series are determined by the boundary conditions. To solve (14) one can apply a method developed for inhomogeneous linear differential equations. For the moment, we assume that the right hand side is fixed (given as χ). We define a "*Greens-function*" by:

$$\left( \Delta + k^2 \right) G\left( \underline{r}, \underline{r}' \right) = \delta\left( \underline{r} - \underline{r}' \right) \qquad (15)$$

We can easily verify that a solution of (15) is given by:

$$G\left( \underline{r}, \underline{r}' \right) = \frac{e^{ik\left| \underline{r} - \underline{r}' \right|}}{4\pi \left| \underline{r} - \underline{r}' \right|} \qquad (16)$$

The meaning of (16) is immediately clear: the scattering from a point-like scatterer (δ-potential) gives a emitted spherical wave.

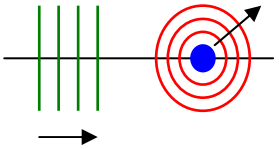

Using the "Greens-function" G(r,r'), a formal solution of the wave equation (14) can be given:

$$\Psi = \Psi^o + \int G(\underline{r},\underline{r}')\,\chi(\underline{r}')\,d^3r' \qquad (17)$$

Here, we have taken the initial conditions of a incident plane wave $\psi^0$ into account. That (17) is indeed a solution of (14) can be easily verified by substituting (17) into (14). If we finally substitute the definition of $\chi$, one obtains:

$$\Psi(\underline{r}) = \psi^o(\underline{r}) + \frac{2m_n}{\hbar^2}\int G(\underline{r},\underline{r}')V(\underline{r}')\Psi(\underline{r}')\,d^3r' \qquad (18)$$

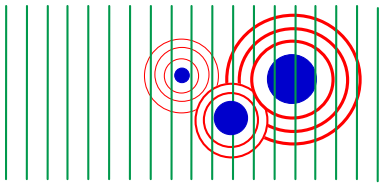

(18) has a simple interpretation: the incident plane wave $\psi^0(\underline{r})$ is superimposed by spherical waves emitted from scattering at positions r'. The intensity of these spherical waves is proportional to the interaction potential V(r') and the amplitude of the wave field at the position r'. To obtain the total scattering amplitude, we have to integrate over the entire sample volume.

However, we still have not solved (14): our solution $\psi$ appears again in the integral in (18). In other words, we have transformed differential equation (14) into an integral equation. The advantage is that for such an integral equation, a solution can be found by iteration. In the zeroth approximation, we neglect the interaction V completely. This gives $\psi = \psi^0$. The next higher approximation for a weak interaction potential is obtained by substituting this solution in the right hand side of (18). The first non-trivial approximation can thus be obtained:

$$\Psi^1(\underline{r}) = e^{i\underline{k}\cdot\underline{r}} + \frac{2m_n}{\hbar^2}\int \frac{\exp\left(ik|\underline{r}-\underline{r}'|\right)}{4\pi|\underline{r}-\underline{r}'|}V(\underline{r}')e^{i\underline{k}\underline{r}'}d^3r' \qquad (19)$$

(19) is nothing else but a mathematical formulation of the well-known *Huygens principle* for wave propagation.

The approximation (19) assumes that the incident plane wave is only scattered once from the potential V(r'). For a stronger potential and larger sample, multiple scattering processes can occur. Again, this can be deduced from the integral equation (18) by further iteration. For simplification we introduce a new version of equation (18) by writing the integral over the "Greens function" as operator **G**:

$$\psi = \psi^o + \mathbf{G}V\psi \tag{20}$$

The so-called *first Born approximation*, which gives the *kinematical scattering theory* is obtained by substituting the wave function ψ on the right hand side by $\psi^0$:

$$\psi^1 = \psi^o + \mathbf{G}V\psi^o \tag{21}$$

This first approximation can be represented by a simple diagram as a sum of an incident plane wave and a wave scattered once from the potential V.

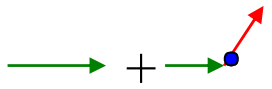

The second approximation is obtained by substituting the solution of the first approximation (21) on the right hand side of equation (20):

$$\begin{aligned}\psi^2 &= \psi^o + \mathbf{G}V\psi^1 \\ &= \psi^o + \mathbf{G}V\psi^o + \mathbf{G}V\mathbf{G}V\psi^o\end{aligned} \tag{22}$$

Or in a diagrammatic form:

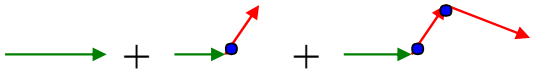

I. e. in the second approximation, processes are being taken into account, in which the neutron is scattered twice by the interaction potential V. In a similar manner, all higher order approximations can be calculated. This gives the so-called *Born series*. For a weak potential and small samples, this series converges rather fast. Often, the first approximation, the kinematic scattering theory, holds very well. This is especially the case for neutron scattering, where the scattering potential is rather weak, as compared to x-ray- or electron- scattering. Due to the strong Coulomb interaction potential, the probability for multiple scattering processes of electrons in solids is extremely high, making the interpretation of electron diffraction experiments very difficult. But even for neutrons, the kinematic scattering theory can break down, for example in the case of Bragg scattering from large ideally perfect single crystals, where the Born series does not converge. The wave equation has to be solved exactly under the boundary conditions given by the crystal geometry. For simple geometries, analytical solutions can be obtained. This is then called the *dynamical scattering theory*. Since for neutrons, the kinematical theory holds in most cases, or multiple scattering events can be corrected for easily, we will no longer discuss dynamical theory in what follows and refer to [3, 5].

Let us return to the first Born approximation (19). According to Fraunhofer, we assume in a further approximation that the size of the sample is significantly smaller than the distance sample-detector. The geometry to calculate the far field limit of (19) is given in Figure 4.

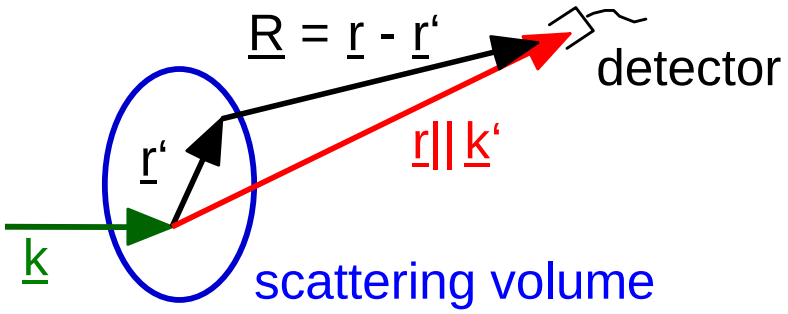


**Figure 4** *Scattering geometry for the calculation of the far field limit at the detector. In the Fraunhofer approximation, we assume that* $|\underline{R}| >> |\underline{r}'|$.

Under the assumption $|\underline{R}| >> |\underline{r}'|$, we can deduce from Figure 4 the following approximation for the emitted spherical wave:

$$\frac{\exp\left(ik\left|\underline{r}-\underline{r}'\right|\right)}{\left|\underline{r}-\underline{r}'\right|} \approx \frac{\exp\left(ik\left(R-\underline{r}'\cdot\hat{\underline{R}}\right)\right)}{R} \approx \frac{\exp(ikR)}{R}\cdot e^{-i\underline{k}'\cdot\underline{r}'} \tag{23}$$

The probability density amplitude for the scattered wave field in the limit of large distances from the sample is thus given by:

$$\Rightarrow \psi^1\left(\underline{R}\right) = e^{i\underline{k}\cdot\underline{R}} + \frac{2m_n}{\hbar^2}\frac{e^{ikR}}{4\pi R}\int V\left(\underline{r}'\right)e^{i\underline{Q}\cdot\underline{r}'}d^3r' \tag{24}$$

This is just the sum of an incident plane wave and a spherical wave emitted from the sample as a whole. The amplitude of the scattered wave is given according to (24):

$$A\left(\underline{Q}\right) = \frac{m_n}{2\pi\hbar^2}\int V\left(\underline{r}\right)e^{i\underline{Q}\cdot\underline{r}}d^3r \sim F\left[V\left(\underline{r}\right)\right] \tag{25}$$

The integral in the above equation is nothing but the transition matrix element of the interaction potential V between the initial and final plane wave states, therefore:

$$\frac{d\sigma}{d\Omega} = \left(\frac{m_n}{2\pi\hbar^2}\right)^2 \left|\left\langle \underline{k}'\middle|V\middle|\underline{k}\right\rangle\right|^2 \tag{26}$$

This formula corresponds to "Fermis Golden Rule" from time-dependent perturbation theory, where the transition probability per time interval from state r to states r' is given by:

$$W_{r'r} = \frac{2\pi}{\hbar}\left|\langle r'|V|r\rangle\right|^2 \cdot \rho(E_{r'}) \tag{27}$$

Here, $\rho(E_{r'})$ denotes the density of states for the final states.

We now allow for inelastic processes, where the sample undergoes a charge of its state from $\alpha$ to $\alpha'$ ($\alpha$ denotes a set of quantum numbers characterizing an eigenstate of the sample). In this case, due to the different length of the wavevectors for incoming and outgoing waves, we have to introduce factors k' and k, which arise from the density of states factor in (27). Since the scattering event must fulfil energy and momentum conservation, we arrive at the double differential cross section:

$$\frac{\partial^2\sigma}{\partial\Omega\partial\omega} = \frac{k'}{k}\left(\frac{m_n}{2\pi\hbar^2}\right)^2 \sum_\alpha p_\alpha \sum_{\alpha'}\left|\langle \underline{k}', \alpha'|V|\underline{k}, \alpha\rangle\right|^2 \cdot \delta(\hbar\omega + E_\alpha - E_{\alpha'}) \tag{28}$$

The summation over $\alpha$ is carried out over all possible initial states $\alpha$ of the systems, weighted with their thermodynamic occupation probability $p_\alpha$. The sum over $\alpha'$ is the sum over all final states allowed by energy conservation, which is guaranteed through the $\delta$-function. $\hbar\omega$ denotes the energy transfer of the neutron to the system. This double differential cross section will be discussed in the following lectures on inelastic scattering.

## 2.3 Coherence

In the above derivation, we assumed plane waves as initial and final states. For a real scattering experiment, this is an unphysical assumption. In the incident beam, a wave packet is produced by collimation and monochromatisation. This wave packet can be described as a superposition of plane waves. As a consequence, the diffraction pattern will be a superposition of patterns for different incident wavevectors $\underline{k}$ and the question arises, which information is lost due to these non-ideal conditions. This "instrumental resolution" is intimately connected with the "coherence" of the beam. Coherence is needed, so that the interference pattern is not significantly destroyed. Coherence requires a phase relationship between the different components of the beam. Two types of coherence have to be distinguished.

- Temporal or longitudinal coherence due to a wavelength spread.

A measure for the longitudinal coherence is given by the length, on which two components of the beam with largest wavelength difference ($\lambda$ and $\lambda + \Delta\lambda$) become fully out of phase. According to the following Figure, this is the case for $l_{\|} = n \cdot \lambda = \left(n - \frac{1}{2}\right)(\lambda + \Delta\lambda)$.

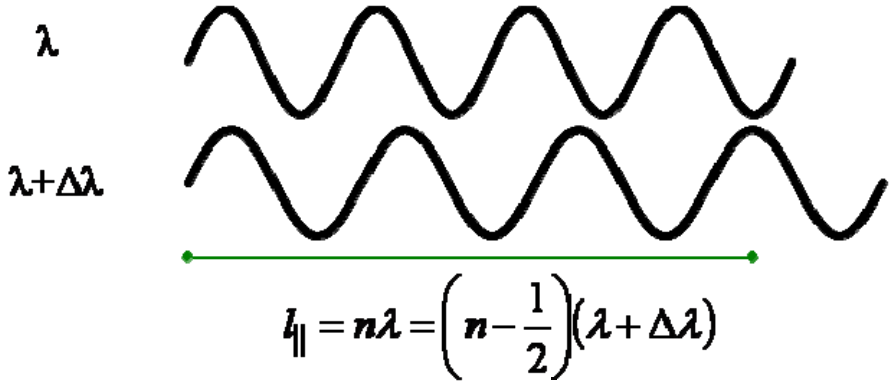


**Figure 5** *A sketch illustrating the longitudinal coherence due to a wavelength spread.*

From this, we obtain the longitudinal coherence length $l_{\parallel}$ as

$$l_{\parallel} = \frac{\lambda^2}{2\Delta\lambda} \tag{29}$$

• Transverse coherence due to source extension

Due to the extension of the source (transverse beam size), the phase relation is destroyed for large source size or large divergence. According to the following Figure, a first minimum occurs for $\frac{\lambda}{2} = d \cdot \sin\theta \approx d \cdot \theta$.

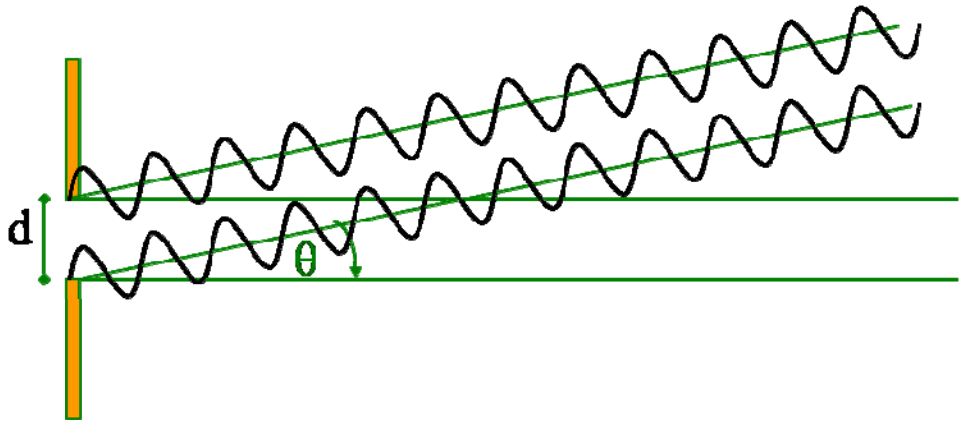


**Figure 6** *A sketch illustrating the transverse coherence due to source extension.*

From this, we obtain the transversal coherence length $l_{\perp}$ as

$$l_{\perp} = \frac{\lambda}{2\Delta\theta} \tag{30}$$

where Δθ is the divergence of the beam. Note that $l_\perp$ can be different along different spatial directions: in many instruments, the vertical and horizontal collimations are different.

Together, the longitudinal and the two transversal coherence lengths define a coherence volume. This is a measure for a volume within the sample, in which the amplitudes of all scattered waves superimpose to produce an interference pattern. Normally, the coherence volume is significantly smaller than the sample size, typically a few 100 Å for neutron scattering, up to μm for synchrotron radiation. Scattering between different coherence volumes within the sample is no longer coherent, i. e. instead of the amplitudes, the intensities of the contributions to the scattering pattern have to be added. This limits the spatial resolution of a scattering experiment to the extension of the coherence volume.

## 2.4 Pair Correlation Functions

After having clarified the conditions under which we can expect a coherent scattering process, let us now come back to the question, which information is accessible from the intensity distribution of a scattering experiment. From (9) we see that the phase information is lost during the measurement of the intensity. For this reason the Fourier transform of the scattering power density is not directly accessible in most scattering experiments (note however that phase information can be obtained in certain cases).

Substituting (8) into (9), we obtain for the magnitude square of the scattering amplitude, a quantity directly accessible in a scattering experiment:

$$I \sim \left| A\left(\underline{Q}\right)\right|^2 \sim \int d^3r' \rho_s\left(\underline{r}'\right) e^{i\underline{Q}\cdot\underline{r}'} \int d^3r\ \rho_s^*\left(\underline{r}\right) e^{-i\underline{Q}\cdot\underline{r}} = \iint d^3r' d^3r\ \rho_s\left(\underline{r}'\right)\rho_s^*\left(\underline{r}\right) e^{i\underline{Q}\cdot\left(\underline{r}'-\underline{r}\right)}$$
$$= \iint d^3R d^3r \rho_s\left(\underline{R}+\underline{r}\right)\rho_s^*\left(\underline{r}\right) e^{i\underline{Q}\cdot\underline{R}} \qquad (31)$$

This shows that the scattered intensity is proportional to the Fourier transform of a function P(R):

$$I\left(\underline{Q}\right) \sim \int d^3R\ P\left(\underline{R}\right) e^{i\underline{Q}\cdot\underline{R}} \qquad (32)$$

This function denotes the so-called *Patterson function* in crystallography or more general the *static pair correlation function:*

$$P\left(\underline{R}\right) = \int d^3r\ \rho_s^*\left(\underline{r}\right)\rho_s\left(\underline{r}+\underline{R}\right) \qquad (33)$$

P(R) correlates the value of the scattering power density at position r with the value at the position r + R, integrated over the entire sample volume. If, averaged over the sample, no correlation exists between the values of the scattering power densities at position r and r+R, then the Patterson function P(R) vanishes. If, however, a periodic arrangement of a pair of atoms

exists in the sample with a difference vector $\underline{R}$ between the positions, then the Patterson function will have an extremum for this vector $\underline{R}$. Thus the Patterson function reproduces all the vectors connecting one atom with another atom in a periodic arrangement.

Quite generally, in a scattering experiment, pair correlation functions are being determined. In a coherent inelastic scattering experiment, we measure the *scattering law S(Q,ω)*, which is the Fourier transform with respect to space and time of the spatial and temporal pair correlation function:

$$\frac{d^2\sigma}{d\omega d\Omega} \sim S\left(\underline{Q},\omega\right) = \frac{1}{2\pi\hbar}\int_{-\infty}^{+\infty} dt\, e^{-i\omega t}\int d^3r\, e^{i\underline{Q}\cdot\underline{r}} G\left(\underline{r},t\right) \tag{34}$$

While the proportionality factor between the double differential cross section and the scattering law depends on the type of radiation and its specific interaction potential with the system studied, the spatial and temporal pair correlation function is only a property of the system studied and independent of our probe:

$$G\left(\underline{r},t\right) = \frac{1}{N}\sum_{ij}\int d^3r' \left\langle \delta\left(\underline{r}'-\underline{r}_j\left(0\right)\right)\cdot\delta\left(\underline{r}'+\underline{r}-\underline{r}_i\left(t\right)\right)\right\rangle = \frac{1}{N}\int d^3r' \left\langle \rho\left(\underline{r}',0\right)\rho\left(\underline{r}'+\underline{r},t\right)\right\rangle \tag{35}$$

Here, the pair correlation function is once expressed as a correlation between the position of N point-like particles (expressed by the delta function) and once by the correlation between the densities at different positions in the sample for different times. In a magnetic system, we scatter from the atomic magnetic moments, which are vector quantities. Therefore, the scattering law becomes a tensor - the Fourier transform of the spin pair correlations (α, ß denote the Cartesian coordinates x, y, z; $\underline{R}_0$ and $\underline{R}_l$ are the spatial coordinates of a reference spin 0 and a spin l in the system)

$$\mathbf{S}^{\alpha\beta}(\underline{Q},\omega) = \frac{1}{2\pi}\sum_{l}\int dt\, e^{i\left[\underline{Q}\left(\underline{R}_l-\underline{R}_0\right)-\omega t\right]}\left\langle S_0^{\alpha}(0) S_l^{\beta}(t)\right\rangle \tag{36}$$

## 2.5 Form-Factor

So far we have not specified the nature of our sample. Now we assume an assembly on N scatterers of finite size, see Figure 7.

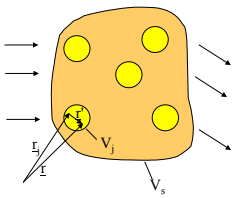


**Figure 7** *Sketch showing the assembly of N scatterers of finite size and defining the quantities needed for the introduction of the form factor.*

These could be atoms in a solid, or colloidal particles in a homogeneous solution. In what follows, we will separate the interference effects from the scattering within one such particle from the interference effects arising from scattering from different particles. With the decomposition of the vector $\underline{r}$ into the centre-of-gravity-vector $\underline{r}_j$ and a vector $\underline{r}'$ within the particle, the scattering amplitude can be written as:

$$\begin{aligned} A &\propto \int_{V_S} d^3r\, \rho_S(\underline{r}) e^{i\underline{Q}\cdot\underline{r}} = \sum_{j=1}^{N} \int_{V_j} d^3r\, \rho_S(\underline{r}) e^{i\underline{Q}\cdot\underline{r}} = \sum_{j=1}^{N} e^{i\underline{Q}\cdot\underline{r}_j} \int_{V_j^0} d^3r'\, \rho_S(\underline{r}') e^{i\underline{Q}\cdot\underline{r}'} \\ \Rightarrow A &\sim \sum_{j=1}^{N} A_j(0) \cdot f_j(\underline{Q})\, e^{i\underline{Q}\cdot\underline{r}_j} \end{aligned} \tag{37}$$

The *form-factor* is defined as the normalised amplitude of scattering from within one particle:

$$f(\underline{Q}) \equiv \frac{\int_{V_j^0} d^3r'\, \rho_s(\underline{r}')\, e^{i\underline{Q}\cdot\underline{r}'}}{\int_{V_j^0} d^3r'\, \rho_s(\underline{r}')} \tag{38}$$

For a homogeneous sphere

$$\rho_S(\underline{r}) = \begin{cases} 0 & |\underline{r}| > R \\ 1 & |\underline{r}| \le R \end{cases} \tag{39}$$

the form-factor can be calculated by using spherical co-ordinates:

$$\Rightarrow f(Q) = 3 \cdot \frac{\sin QR - QR \cdot \cos QR}{(QR)^3} \tag{40}$$

The function (40) is plotted in Figure 8. In forward direction, there is no phase difference between waves scattered from different volume elements within the sample (note: we assume the Fraunhofer approximation and work in a far field limit). The form-factor takes its maximum value of one. For finite scattering angles $2\theta$, the form-factor drops due to destructive interference from various parts within one particle and finally for large values of the momentum transfer shows damped oscillations around 0 as a function of QR.

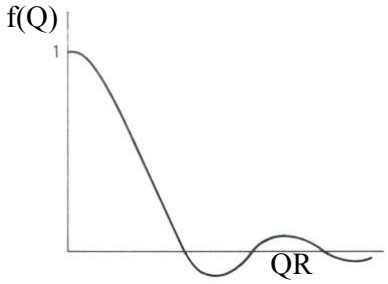


**Figure 8** *Form-factor for a homogeneous sphere according to (40).*

## 2.6 Scattering from a Periodic Lattice in Three Dimensions

As an example for the application of (8) and (9), we will now discuss the scattering from a three dimensional lattice of point-like scatterers. As we will see later, this situation corresponds to the scattering of thermal neutrons from a single crystal. More precisely, we will restrict ourselves to the case of a Bravais lattice with one atom at the origin of the unit cell. To each atom we attribute a scattering power $\alpha$. The single crystal is finite with N, M and P periods along the basis vectors $\underline{a}$, $\underline{b}$ and $\underline{c}$. The scattering power density, which we have to use in (8) is a sum over $\delta$-functions for all scattering centres:

$$\rho_s\left(\underline{r}\right) = \sum_{n=0}^{N-1}\sum_{m=0}^{M-1}\sum_{p=0}^{P-1} \alpha \cdot \delta\left(\underline{r} - \left(n \cdot \underline{a} + m \cdot \underline{b} + p \cdot \underline{c}\right)\right) \tag{41}$$

The scattering amplitude is calculated as a Fourier transform:

$$A\left(\underline{Q}\right) \sim \alpha \sum_{n=0}^{N-1} e^{in\underline{Q}\cdot\underline{a}} \sum_{m=0}^{M-1} e^{im\underline{Q}\cdot\underline{b}} \sum_{p=0}^{P-1} e^{ip\underline{Q}\cdot\underline{c}} \tag{42}$$

Summing up the geometrical series, we obtain for the scattered intensity:

$$I\left(\underline{Q}\right) \sim \left| A\left(\underline{Q}\right)\right|^2 = \left|\alpha\right|^2 \cdot \frac{\sin^2 \frac{1}{2} N\underline{Q}\cdot\underline{a}}{\sin^2 \frac{1}{2}\underline{Q}\cdot\underline{a}} \cdot \frac{\sin^2 \frac{1}{2} M\underline{Q}\cdot\underline{b}}{\sin^2 \frac{1}{2}\underline{Q}\cdot\underline{b}} \cdot \frac{\sin^2 \frac{1}{2} P\underline{Q}\cdot\underline{c}}{\sin^2 \frac{1}{2}\underline{Q}\cdot\underline{c}} \tag{43}$$

The dependence on the scattering vector $\underline{Q}$ is given by the so-called *Laue function*, which separates according to the three directions in space. One factor along one lattice direction $\underline{a}$ is plotted in Figure 9.

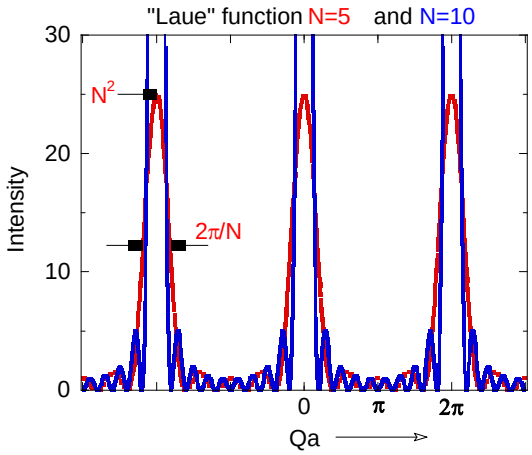


**Figure 9** *Laue function along the lattice direction a for a lattice with five and ten periods, respectively.*

The main maxima occur at the positions $Q = n \cdot 2\pi/a$. The maximum intensity scales with the square of the number of periods $N^2$, the half width is given approximately by $\Delta Q = 2\pi/(N \cdot a)$. The more periods contribute to coherent scattering, the sharper and higher are the main peaks. Between the main peaks, there are N-2 site maxima. With increasing number of periods N, their intensity becomes rapidly negligible compared to the intensity of the main peaks. The main peaks are of course the well known *Bragg reflections*, which we obtain when scattering from a crystal lattice. From the position of these Bragg peaks in momentum space, the metric of the unit cell can be deduced (lattice constants a, b, c and unit cell angles $\alpha$, $\beta$, $\gamma$). The width of the Bragg peaks is determined by the size of the coherently scattering volume (parameters N, M, and P) - and some other factors for real experiments (resolution, mosaic distribution, internal strains, ...).

# 3 Probes for Scattering Experiments in Condensed Matter Science

In this chapter, we will discuss which type of radiation is suitable for condensed matter investigations. For each radiation, we will then discuss the relevant interaction processes with matter separately.

## 3.1 Suitable Types of Radiation

A list of requirements for the type of radiation used in condensed matter investigations will look as follows:

(1) The achievable spatial resolution should be in the order of the inter-particle distances, which implies (see section 2.1) that the wavelength $\lambda$ is in the order of the inter-particle distance L.

(2) If we want to study volume effects, the scattering has to originate from the bulk of the sample, which implies that the radiation should be at most weakly absorbed within matter.

(3) For a simple interpretation of the scattering data within the Born approximation (see chapter 2), multiple scattering effects should be negligible, i. e. the interaction of the radiation with matter should be weak.

(4) For the sake of simplicity, the probe should have no inner degrees of freedom, which could be excited during the scattering process (i. e. avoid beams of molecules, which have internal vibrational or rotational degrees of freedom).

(5) To study magnetic systems, we need a probe which interacts with the atomic magnetic moments in the sample.

(6) If, in addition to structural studies, we want to investigate elementary excitations, we would like the energy of the probe to be in the order of the excitation energies, so that the energy change during the scattering process is easily measurable.

This list of requirements leads us to some standard probes in condensed matter research. First of all, electromagnetic radiation governed by the Maxwell equations can be used. Depending on the resolution requirements, we will use x-rays with wavelength $\lambda$ about 0.1 nm to achieve atomic resolution or visible light ($\lambda \sim 350$ - 700 nm) to investigate e. g. colloidal particles in solution. Besides electromagnetic radiation, particle waves can be used. It turns out that thermal neutrons with a wavelength $\lambda \sim 0.1$ nm are particularly well adapted to the above list of requirements. The neutron beams are governed by the Schrödinger equation of quantum mechanics. An alternative is to use electrons, which for energies of around 100 keV have wavelengths in the order of 0.005 nm. As relativistic particles, they are governed by the Dirac equation of quantum mechanics. The big drawback of electrons as a condensed matter probe is the strong Coulomb interaction with the electrons in the sample. Therefore neither absorption, nor multiple scattering effects can be neglected. However the abundance of electrons and the relative ease to produce optical elements makes them very suitable for imaging purposes (electron microscopy). Electrons, but also atomic beams are also very powerful tools for surface science: due to their strong interaction with matter, both types of radiation are very surface sensitive. Low Energy Electron Diffraction LEED and Reflection High Energy Electron Diffraction RHEED are both used for in-situ studies of the crystalline structure during thin film growth, e.g. with Molecular Beam Epitaxy MBE. In what follows we will concentrate on the two probes, which are best suited for bulk studies on an atomic scale: x-rays and neutrons. For both probes, we will derive the scattering cross sections for the main interaction processes with matter.

## 3.2 The Scattering Cross Section for X-rays: Thomson Scattering, Anomalous Charge Scattering and Magnetic X-ray Scattering

X-rays are electromagnetic waves with wavelengths typically shorter than 1 nm. For electromagnetic waves, the relation between energy and wavelength is given by

$$E = h\nu = \frac{h \cdot c}{\lambda} \tag{44}$$

or in practical units

$$E\left[keV\right] = \frac{1.24}{\lambda\left[nm\right]} \tag{45}$$

i. e. x-rays with a wavelength of 0.1 nm have an energy of 12.4 keV. The corresponding elementary particle - the photon - is massless, has no charge, but spin 1. For a massless particle of spin 1, two polarisation states can be distinguished, corresponding to left or right circular polarised light. According to de Broglie, the relation between momentum p and wavelength λ is given by

$$\underline{p} = \hbar\underline{k};\ p = h/\lambda \tag{46}$$

In a classical picture, the main interaction of x-rays with matter resulting in coherent scattering is due to the Coulomb force exerted by the oscillating electric field $E(\underline{r},t)$ on the electrons in the sample. Here, we first discuss processes at x-ray energies far above the energies of the absorption edges, where electron binding energies can be neglected and where we can assume the electrons to behave like free electrons. Then the Coulomb force from the electrical field gives rise to a driven harmonic oscillation of the electrons with irradiation of electric dipole radiation. This process is called classical *Thomson scattering*. It is coherent as there is a phase relation between waves scattered from different positions within the sample. Note that in a quantum mechanical treatment, due to energy and momentum conservation, there cannot be any coherent elastic scattering of a photon from a free electron. The incoherent process, where the photon transfers energy and momentum to a free electron in the sample is called *Compton scattering*. Therefore, only a fraction of the scattering from the bound electrons of an atom gives rise to Thomson charge scattering. It can be shown that this fraction is given by the atomic form factor [6]. While coherent charge scattering is the basis for any x-ray structure determination, there has to be also an interaction of the x-rays with the magnetic moments in the solid, since x-rays are an electro*magnetic* wave. However, as we will see below, magnetic x-ray scattering at energies above the absorption edges is a relativistic correction to charge scattering and about 6 orders of magnitude weaker. It can only be exploited since the advent of synchrotron x-ray sources which provide the necessary brilliant x-ray beams. As we have learned in the lecture on synchrotron radiation sources, these beams are not only well collimated and intense, but also polarized and their energy can be varied. If the energy of such a beam is tuned to one of the absorption edges of an atom in the sample, additional scattering channels are opened. At the absorption edge, photoelectric absorption occurs, where electrons are promoted from core levels into empty states above the Fermi level. Photons taking part in photoelectric absorption are lost for the scattering experiment. However, as we will see below, the incident photons can also give rise to virtual transitions between core levels and states above the Fermi level and back to the core states with irradiation of x-rays with the same energy as the initial ones. For charge scattering, this

*anomalous scattering* gives rise to additional terms in the form factor, which can be used for contrast variation, e.g. to enhance the scattering contrast between neighboring elements. Anomalous scattering is also sensitive to local anisotropies, e.g. the arrangement of orbitals, so called orbital order. In a magnetic solid, resonant magnetic scattering (so called *resonance exchange scattering XRES*) with large enhancement factors as compared to *non-resonant magnetic scattering* can occur at the absorption edges of the magnetic elements. To obtain the cross section for all these different scattering processes, we have to introduce the quantum mechanical formulation of the interaction between electromagnetic waves and the electrons in a solid.

For a calculation of the cross-section for x-ray scattering including the magnetic terms we follow a presentation given by Blume [7, 9] and Blume and Gibbs [8] based on a non-relativistic treatment in second order perturbation theory. We start with the Hamiltonian for electrons in a quantized electromagnetic field:

$$\begin{aligned}\mathbf{H} &= \sum_j \frac{1}{2m}(\underline{\mathbf{P}}_j - \frac{e}{c}\underline{\mathbf{A}}(\underline{\mathbf{r}}_\mathbf{j}))^2 + \sum_{ji}\mathbf{V}(\mathbf{r_{ij}}) - \frac{e\hbar}{mc}\sum_j \underline{\mathbf{s}}_\mathbf{j}\cdot\underline{\nabla}\times\underline{\mathbf{A}}(\underline{\mathbf{r}}_\mathbf{j}) \\ &- \frac{e\hbar}{2(mc)^2}\sum_j \underline{\mathbf{s}}_\mathbf{j}\cdot\underline{\mathbf{E}}(\underline{\mathbf{r}}_\mathbf{j})\times(\underline{\mathbf{P}}_\mathbf{j} - \frac{e}{c}\underline{\mathbf{A}}(\underline{\mathbf{r}}_\mathbf{j})) + \sum_{k\lambda}\hbar\omega_k(\mathbf{c}^+(\underline{\mathbf{k}}\boldsymbol{\lambda})\mathbf{c}(\underline{\mathbf{k}}\boldsymbol{\lambda}) + \frac{1}{2})\end{aligned} \tag{47}$$

Here, the first term corresponds to the kinetic energy of the electrons in the electromagnetic field, represented by the vector potential $\underline{\mathbf{A}}(\underline{\mathbf{r}})$, the second term corresponds to the Coulomb interaction between the electrons, the third term to the Zeeman energy $-\underline{\mu}\cdot\underline{H}$ of the electrons with spin $\underline{s}_j$, the fourth term to the spin-orbit coupling and the final term to the self energy of the electromagnetic field. The vector potential $\underline{\mathbf{A}}(\underline{\mathbf{r}})$ in (47) is linear in photon creation and annihilation operators, $\mathbf{c}^+(\underline{\mathbf{k}}\boldsymbol{\lambda})$ and $\mathbf{c}(\underline{\mathbf{k}}\boldsymbol{\lambda})$ and is given in a plane wave expansion by:

$$\underline{\mathbf{A}}(\underline{\mathbf{r}}) = \sum_{\underline{q}\sigma}\left(\frac{2\pi\hbar c^2}{V\omega_q}\right)^{\frac{1}{2}}\times[\underline{\varepsilon}(\underline{q}\sigma)\mathbf{c}(\underline{\mathbf{q}}\boldsymbol{\sigma})e^{i\underline{q}\cdot\underline{r}} + \underline{\varepsilon}^*(\underline{q}\sigma)\mathbf{c}^+(\underline{\mathbf{q}}\boldsymbol{\sigma})e^{-i\underline{q}\cdot\underline{r}}] \tag{48}$$

Here V is a quantization volume and $\underline{\varepsilon}(\underline{q}\sigma)$ is the unit polarization vector corresponding to a wave with wavevector $\underline{q}$ of polarization state $\sigma$. Two polarization states $\sigma = 1,\ 2$ of the photons have to be distinguished. As a basis, we can either use linear polarization in two perpendicular directions or left and right circular polarization. Since $\underline{\mathbf{A}}(\underline{\mathbf{r}})$ is linear in the $\mathbf{c}^+$ and $\mathbf{c}$-operators, scattering occurs in second order for terms linear in $\underline{\mathbf{A}}$ and in first order for quadratic terms. We do not want to reproduce the calculation given in [7] in detail. The Hamiltonian (47) is written as a sum

$$\mathbf{H} = \mathbf{H_0} + \mathbf{H_r} + \mathbf{H'} \tag{49}$$

where $\mathbf{H_0}$ contains only the degrees of freedom of the electron system, $\mathbf{H_r}$ is the Hamiltonian for the quantized electromagnetic field and $\mathbf{H'}$ corresponds to the interaction between the

electrons and the radiation field. Scattering cross-sections are calculated by assuming that initially the solid is in a quantum state |a>, which is an eigenstate of $\mathbf{H_0}$ with energy $E_a$, and that there is a single photon present. Following Fermi's Golden Rule up to second order perturbation theory, we then calculate the probability of a transition induced by the interaction Hamiltonian **H'** to a state |b> with photon $\underline{k}'\lambda'$. For elastic scattering |b> = |a>. The transition probability per unit time can be calculated by the Golden Rule to second order perturbation theory. The fact that we have to go to second order perturbation theory for terms linear in $\underline{\mathbf{A}}$ immediately implies that besides the so-called non-resonant magnetic x-ray scattering, resonance phenomena will appear due to the energy denominator found in second order perturbation theory (compare the Breit-Wigner-formula for resonant scattering of the neutron from a nucleus). Here we will just quote the final result of this calculation: at moderately high x-ray energies and far away from all absorption edges of the elements in the sample, the elastic cross-section for scattering of photons with incident polarization ε into a state of final polarization ε' can be written as:

$$\left.\frac{d\sigma}{d\Omega}\right|_{\varepsilon\to\varepsilon'} = \left[\frac{e^2}{mc^2}\right]^2 \cdot \left|\left\langle f_C \right\rangle_{\varepsilon'\varepsilon} + i\frac{\lambda_C}{d}\left\langle f_M \right\rangle_{\varepsilon'\varepsilon}\right|^2 \tag{50}$$

Here $r_e = e^2/mc^2$ = 2.818 fm denotes the classical electron radius, $\lambda_C$ = h/mc = 2.426 pm the Compton length of an electron. The scattering amplitudes $\langle f_C \rangle$ and $\langle f_M \rangle$ are given as matrices which describe the polarization dependencies of charge and magnetic scattering, respectively. Here we discuss the case of linear polarization, described by unit vectors perpendicular to the wave vectors of incident and scattered photons, $\underline{k}$ and $\underline{k}'$. σ-polarization corresponds to the basis vector perpendicular to the scattering plane, π-polarization corresponds to the vectors in the $\underline{k}$, $\underline{k}'$ plane. The basis vectors for the components of the magnetic moment of the sample and for the polarization states are defined as follows, see Figure 10:

$$\begin{aligned}
\hat{u}_1 &= (\underline{k}+\underline{k}')/|\underline{k}+\underline{k}'| \\
\hat{u}_2 &= (\underline{k}'\times\underline{k})/|\underline{k}'\times\underline{k}| \equiv \underline{\sigma} \equiv \underline{\sigma}' \\
\hat{u}_3 &= (\underline{k}'-\underline{k})/|\underline{k}'-\underline{k}| = \underline{Q}/Q \\
\underline{\pi} &= \hat{\underline{k}}\times\underline{\sigma} \quad ; \quad \underline{\pi}' = \hat{\underline{k}}'\times\underline{\sigma}'
\end{aligned} \tag{51}$$

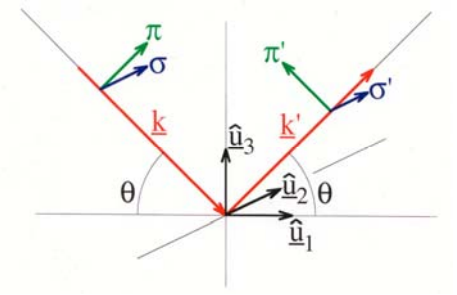


**Figure 10** *Illustration of the definition of the co-ordinate system and the basis vectors used to describe the polarization dependence of x-ray scattering.*

In this basis the matrices in (50) can be written as

- $\langle f_M \rangle$ for the magnetic part:

| $to \backslash from$ | $\sigma$ | $\pi$ |
|---|---|---|
| $\sigma'$ | $S_2 \cdot \cos\theta$ | $\left[(L_1 + S_1)\cdot\cos\theta + S_3 \cdot \sin\theta\right]\cdot\sin\theta$ |
| $\pi'$ | $\left[-(L_1 + S_1)\cdot\cos\theta + S_3 \cdot \sin\theta\right]\cdot\sin\theta$ | $\left[2L_2 \cdot \sin^2\theta + S_2\right]\cdot\cos\theta$ |

(52)

- $\langle f_C \rangle$ for charge scattering:

| $to \backslash from$ | $\sigma$ | $\pi$ |
|---|---|---|
| $\sigma'$ | $\rho(\underline{Q})$ | 0 |
| $\pi'$ | 0 | $\rho(\underline{Q})(\cos 2\theta)$ |

(53)

Here $S_i = S_i(\underline{Q})$ and $L_i = L_i(\underline{Q})$ (i=1, 2, 3) denote the components of the Fourier transform of the magnetization density due to the spin and orbital angular momentum, respectively. $\rho(\underline{Q})$ denotes the Fourier transform of the electronic charge density distribution.

As can be seen from (50), magnetic scattering is a relativistic correction to charge scattering. For coherent elastic Bragg scattering, the ratio between the magnetic and the charge amplitude is determined by the momentum transfer and therefore we have written the pre-factor for the magnetic amplitude in the cross-section (50) as $\lambda_C/d$ which emphasizes that for a given Bragg reflection the ratio between magnetic and charge scattering is virtually independent of photon energy, at least to within the approximations leading to (50).

(50) contains three terms: pure Thomson-scattering, purely magnetic scattering and an interference term. The latter becomes important if charge- and magnetic scattering occur at the same position in reciprocal space, which is the case for ferromagnets. Note, however, that the prefactor "i" in front of the magnetic scattering amplitude means that magnetic scattering is shifted in phase by $\pi/2$ as compared to charge scattering. Therefore if both amplitudes, $\langle f_C \rangle$ and $\langle f_M \rangle$ are real, the interference term vanishes. The interference can only be observed, if one of the amplitudes contains an imaginary part (e. g. non centrosymmetric structures or photon energy close to an absorption edge for charge scattering) or if circular polarized radiation is used. The importance of the interference term for ferromagnets becomes evident, if we consider the ratio between magnetic and charge scattering amplitudes. An estimate for this ratio can be given as:

$$\frac{\langle f_M \rangle}{\langle f_C \rangle} \sim \frac{\lambda_C}{d} \cdot \frac{N_M f_M}{N \cdot f} \cdot \langle S \rangle \qquad (54)$$

Here, $N(N_M)$ and $f(f_M)$ denote the number and the form factor of all (the magnetic) electrons, $\langle S \rangle$ the expectation value of the spin quantum number. Using appropriate values for the pa-

rameters in (54), one finds that the amplitude for magnetic scattering is typically three orders of magnitude smaller than the amplitude of charge scattering, resulting in an intensity ratio of $10^{-6}$ between pure magnetic and pure charge scattering. It is not practical to measure a $10^{-6}$ effect in intensities. Therefore for ferromagnets, where charge and magnetic scattering coincide in reciprocal space, the interference term between charge and magnetic scattering is the leading term after charge scattering. To measure it, one periodically changes the direction of the magnetization (or the incident photon polarization) to change the sign of the interference term and thus to separate this term from the pure charge scattering.

(52) and (53) show that magnetic scattering can be discriminated from charge scattering by a polarization analysis experiment, where the off-diagonal terms $\sigma \rightarrow \pi'$ or $\pi \rightarrow \sigma'$ are being measured. Finally, (52) shows that the spin and orbital contributions have different angular- and polarization dependencies and can therefore be distinguished in principle.

We have sketched a derivation of the non-resonant magnetic scattering cross sections starting from non-relativistic quantum mechanics and applying perturbation theory up to second order. It should be noted that the scattering cross-section can also be derived in a purely classical theory [10]. It turns out that the classical calculation reproduces the quantum mechanical cross-section for the spin part, but not for the orbital part. De Bergevin and Brunel [11] have drawn a simple diagram, representing the various interaction processes in such a classical model. This diagram is reproduced as Figure 11.

The first process shown in Figure 11 is the classical charge or Thompson scattering: an electromagnetic wave is incident on a free electron and due to the Coulomb force between the electric field vector and the charge of the electron, the electron is accelerated into a harmonic oscillation and re-radiates electric dipole radiation. The three other processes only appear if the electron carries a spin momentum, i. e. these processes give rise to magnetic x-ray scattering. The second process in Figure 11 arises from the same Coulomb interaction with the incident electromagnetic wave. The accelerated spin moment gives rise to re-radiation of magnetic quadrupole radiation. In the third and fourth process of Figure 11, the interaction with the incident electromagnetic field is between the spin moment and the magnetic field vector.

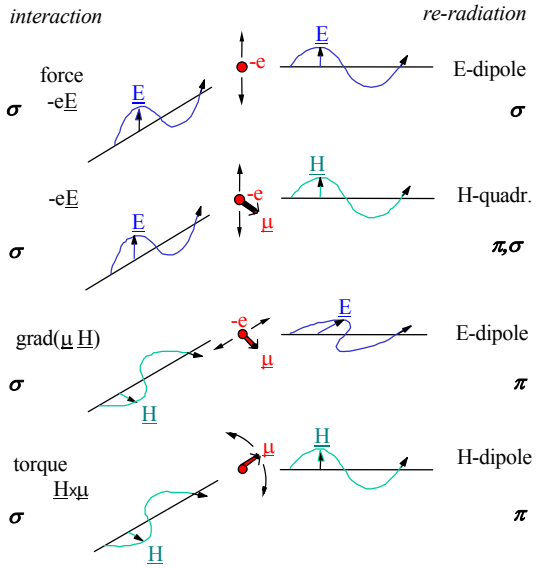


**Figure 11** *Illustration of the processes leading to scattering of x-rays by the charge (top) and the spin moment (bottom three) of the electron in a classical picture (from [11]).*

From Figure 11, the polarization dependence of charge and magnetic scattering becomes immediately evident. In charge scattering, the polarization of the incident wave is conserved. From our simple classical pictures, it is immediately evident that the matrix (53) has to be diagonal. The cos 2θ factor for $\pi \rightarrow \pi$'-scattering is simply explained by the projection of the acceleration vector onto a plane perpendicular to the observation direction. Figure 11 shows that in contrast to charge scattering, the polarization can indeed change for magnetic x-ray scattering. Therefore the existence of off-diagonal terms in the matrix (52) can easily be motivated from the classical picture, Figure 11. Polarization analysis allows us to clearly distinguish charge and magnetic scattering.

If the x-ray energy is tuned to the absorption edge of magnetic elements, resonance phenomena occur due to second order perturbation theory [9]:

$$\frac{d\sigma}{d\Omega} \sim \sum_c \frac{< a \,|\, \mathbf{O}^+(\underline{k}') \,|\, c >< c \,|\, \mathbf{O}(\underline{k}) \,|\, a >}{E_a - E_c + \hbar\omega - i\Gamma/2} \tag{55}$$

Here |c> denotes an intermediate excited state with energy $E_c$, $\hbar\omega$ the photon energy and $\Gamma$ the level width of the excited state due to the finite lifetime $(\Gamma \cdot \tau \approx \hbar)$. The operator $\mathbf{O}(\underline{k})$ is given by the expression:

$$\underline{\mathbf{O}}(\underline{k}) = \sum_i e^{i\underline{k}\cdot\mathbf{r}_i} (\underline{\mathbf{P}}_i - i\hbar(\underline{k} \times \underline{\mathbf{s}}_i)) \tag{56}$$

(55) gives rise to anomalous dispersion, i. e. an energy dependence of the charge scattering, as well as to resonant magnetic scattering. The operator (56) can be expanded in a multipole series. It turns out that in the x-ray regime, the spin and orbital contributions can be neglected in most cases, and only the electric multipole terms have to be retained. These electric multipole (predominantly dipole and quadrupole) operators induce virtual transitions between core levels and unoccupied states above the Fermi energy with subsequent reemission of a photon. These processes become sensitive to the magnetic state in exchange split bands due to the difference in occupation of minority and majority bands leading to so called *resonance exchange scattering XRES* [12] as illustrated schematically in Figure 12.

Due to the resonance denominator in (55), resonance enhancements occur at the absorption edges of the magnetic elements. Therefore XRES can provide large intensity gains for magnetic x-ray scattering. It also allows a spectroscopy of the exchange split empty states above the Fermi level. Moreover, it renders magnetic diffraction sensitive to the magnetic species since resonance enhancements occur only close to the absorption edges, which have different energies for all elements.

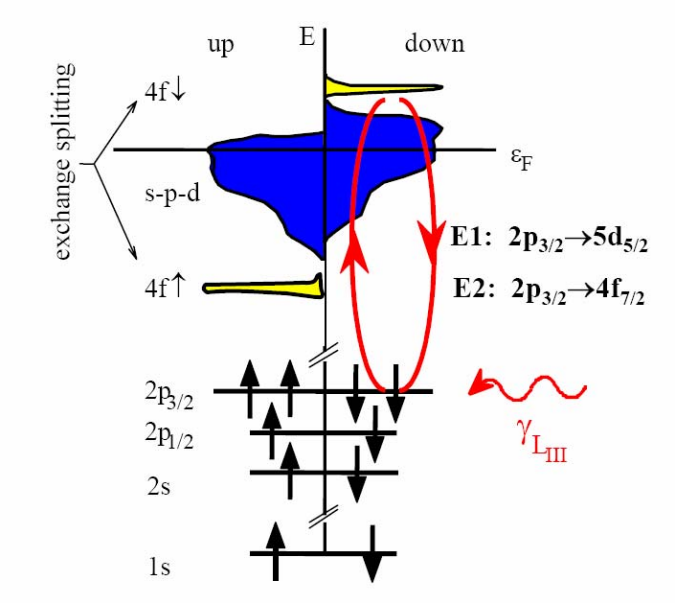


**Figure 12** *Schematic illustration of the second order perturbation process leading to XRES in the case of a lanthanide metal, e. g. a $Gd^{3+}$ - ion.*

Let us come back to the explicit form of the cross-section, including resonant magnetic scattering. We start from (55), which gives the general form of the cross-section for anomalous scattering. In what follows, we will neglect the spin dependent part of the operator (56) and limit ourselves to electric dipole transitions. Detailed derivations are given in [9], [12] and the polarization dependence, also for the case of electric quadrupole transitions, is discussed in [13]. Anomalous scattering becomes relevant close to the absorption edges of the elements. Then, an energy dependent amplitude has to be added to the expression (50) for the scattering cross-section. In dipole approximation, this amplitude reads:

$$f_{res}^{E1}(E) = f_o(E) + f_{circ}(E) + f_{lin}(E) \tag{57}$$

with

$$\begin{aligned} f_0(E) &= (\underline{\varepsilon}' \cdot \underline{\varepsilon})\,[F_{+1}^1 + F_{-1}^1] \\ f_{circ}(E) &= i(\underline{\varepsilon}' \times \underline{\varepsilon}) \cdot \underline{m}\,[F_{-1}^1 - F_{+1}^1] \\ f_{lin}(E) &= (\underline{\varepsilon}' \cdot \underline{m})(\underline{\varepsilon} \cdot \underline{m})[2F_0^1 - F_{+1}^1 - F_{-1}^1] \end{aligned} \tag{58}$$

$f_0$ is independent of the magnetic state (i. e. the conventional anomalous charge scattering), while $f_{circ}$ and $f_{lin}$ are the amplitudes connected for the special case of forward scattering with circular and linear dichroism, respectively. All three amplitudes have different polarization properties. $f_{circ}$ depends linear on the magnetic moment $\underline{m}$, while $f_{lin}$ depends quadratic on $\underline{m}$. Therefore for antiferromagnets, only $f_{circ}$ gives a contribution at positions in reciprocal space

separated from the main charge reflections by the magnetic propagation vector. Finally, for a simple excitation into one atomic-like level, the energy dependence of the amplitudes is contained in the oscillator strengths

$$F_M^1 = \frac{\alpha_M}{(\omega - \omega_{res}) - i\Gamma/2\hbar} \tag{59}$$

Here $\omega$ denotes the photon energy, $\omega_{res}$ the position of the absorption edge and $\Gamma$ the resonance width. The phenomenological parameter $\alpha_M$ gives a measure for the amplitude of the resonance and stands for the product of the transition matrix elements.

(58) shows that XRES can change the polarization of the incident photons. To give an example: while $f_{circ}$ vanishes for $\sigma \rightarrow \sigma'$ scattering, a polarization change $\sigma \rightarrow \pi'$ can occur, depending on the direction of m. In fact, similar resonant scattering processes involving a polarization change are possible for anomalous anisotropic charge scattering. It was derived in [9] from general symmetry arguments that a local anisotropy of the intermediate valence states can give rise to $\sigma \rightarrow \pi'$ scattering. For non-resonant x-ray scattering, atoms appear to be mainly spherical symmetric since most of their electrons are in closed shells. In contrast, during a resonant scattering experiment, the electrons are virtually promoted into the valence states as intermediate states, which experience the local anisotropies. Due to the resonance enhancement, anomalous scattering becomes much more sensitive to these local anisotropies, as already described by Templeton and Templeton [14]. An example is shown in Figure 13: the apparent unit cell is smaller in the case of non-resonant scattering, where the atoms appear to be spherical symmetric. This means that for resonant scattering, additional superstructure reflections appear if the x-ray energy is tuned to the relevant absorption edge. From these superstructure reflections, the orbital ordering pattern can be deduced as will be discussed in more detail in a subsequent lecture.

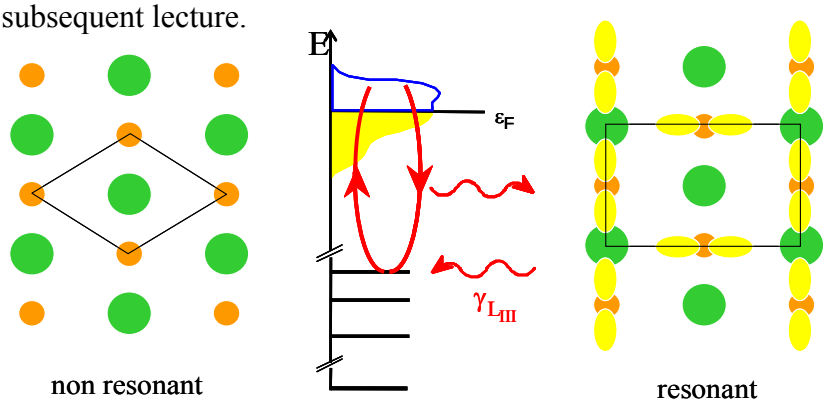


**Figure 13** *Schematic two dimensional illustration of non resonant and resonant x-ray scattering from an imaginary crystalline compound of two atoms (green and orange) together with an illustration of the resonant charge scattering process. The black lines in the Figures on the left and on the right indicate the unit cells corresponding to the periodicity seen by the x-rays in the case of non-resonant and resonant scattering, respectively. These unit cells differ since the atoms appear spherical symmetric for non-resonant scattering, while orbital order is seen, if the energy of the x-rays is tuned to the relevant absorption edge of the "orange" atoms. If the resonant scattering process involves electronic states taking part in the orbital order, this order becomes visible due to resonance enhancement.*

## 3.3 The Scattering Cross Section for Neutrons: Nuclear and Magnetic Scattering

We mentioned in the introduction that neutron beams provide a particularly useful probe for condensed matter investigations. The neutron is an elementary particle, a nucleon, consisting of three valance quarks, which are hold together by gluons. It thus has an internal structure, which, however, is irrelevant for condensed matter physics, since the energy scales involved in internal excitations are much too high. Keeping in mind the difference in lengths scales (diameter of an atom: about 0.1 nm = $10^{-10}$ m; diameter of a neutron: about 1 fm = $10^{-15}$ m), we can safely consider the neutron as a point-like particle without internal structure for our purposes. Due to the weak interaction, the neutron is not a stable particle. A free neutron undergoes a β-decay after an average lifetime of about 15 minutes:

$$n \xrightarrow{15\,\mathrm{min}} p + e^- + \bar{\nu} \qquad \text{weak interaction} \tag{60}$$

This leaves ample time for scattering investigations. In contrast to the massless photon, the neutron has a mass m of about one atomic mass units ~ 1.675 · $10^{-27}$ kg. The finite neutron mass is comparable to the mass of a nucleus and thus an appreciable amount of energy can be transferred during the scattering process. The neutron is a chargeless particle and thus does not show the strong Coulomb interaction with matter. This results in large penetration depths. The neutron has a nuclear spin 1/2 giving rise to a magnetic dipolar moment of

$$\mu_n = \gamma \mu_N; \quad \gamma = 1.91; \quad \mu_N = 5.05 \cdot 10^{-27} J/T \tag{61}$$

Due to this magnetic moment, the neutron can interact with the magnetic field of unpaired electrons in a sample leading to strong magnetic scattering. Thus magnetic structures and excitations can be studied by neutron scattering. To calculate the interference effects during the scattering process, a neutron has to be described as a matter wave with momentum

$$\underline{p} = m \cdot \underline{v} = \hbar \underline{k} = h/\lambda \tag{62}$$

and energy

$$E = \frac{1}{2} m v^2 = \frac{\hbar^2 k^2}{2m} = \frac{h^2}{2m\lambda^2} \equiv k_B T_{eq} \tag{63}$$

where $\underline{v}$ is the velocity of the neutron and $T_{eq}$ defines the temperature equivalent of the kinetic energy of the neutron. In practical units:

$$\lambda[nm] = \frac{400}{v[m/s]}$$
$$E[meV] = \frac{0.818}{\lambda^2[nm]} \tag{64}$$

Let us consider the example of so-called *thermal neutrons*, which are defined by $T_{eq} \sim 300$ K. According to (63), their wavelength is 0.18 nm, matching perfectly the distance between atoms. The energy of thermal neutrons is around 25 meV, which matches well the energy of elementary excitations, such as spin waves (magnons) or lattice vibrations (phonons). Together with the usually large penetration depths (charge = 0) and the magnetic interaction, these properties make neutrons so extremely useful for condensed matter investigations.

We will now look at the neutron scattering cross section in some more detail. The dominant interactions of the neutron with matter are the magnetic dipole interaction of the neutron with the magnetic field of unpaired electrons, which we will discuss below, and the strong interaction of the neutron with the nuclei. To calculate the cross section for neutron scattering, we are looking for a pertubative solution of the Schrödinger equation for the system "sample plus neutron beam". Here we cannot reproduce the full derivation of the form of the cross section and have to refer to [1, 2, 4, 15]. As we have seen in chapter 2.2, an elegant way is the expansion into a *Born series*, which separates single, double, triple etc. scattering events. For a sufficient weak interaction, we can neglect multiple scattering events and write the cross section in the *first Born approximation* (28)*:*

$$\frac{\partial^2\sigma}{\partial\Omega\partial\omega} = \frac{k'}{k}\left(\frac{m_n}{2\pi\hbar^2}\right)^2 \sum_a P_\alpha \sum_{a'} \left|\left\langle \underline{k}',\alpha' \middle| V \middle| \underline{k},\alpha \right\rangle\right|^2 \delta\left(\hbar\omega + E_\alpha - E_{\alpha'}\right) \tag{65}$$

The various terms in this cross section can be understood as follows (compare (28)). The δ-function ensures energy conservation: the energy transfer onto the neutron $\hbar\omega$ has to be equal to the energy change within the sample $E_{\alpha'} - E_\alpha$. The term in front of the δ-function can be interpreted in terms of *Fermis' Golden Rule.* It's the magnitude square of the transition matrix element of the interaction potential V (nucleus ↔ neutron) between the initial state of the system (neutron with wave vector $\underline{k}$, sample in the quantum state a) and the final state (neutron with wave vector $\underline{k}'$, sample in the state a'). In general, neither the initial nor the final state of the sample are pure states. Therefore we have to sum over all processes leading to different final states, but also to sum over the initial states with a weight $P_\alpha$ corresponding to the thermodynamical occupation of state a of the sample. Finally the prefactor k'/k results from the density-of-state consideration in Fermis' Golden Rule.

## 3.4 Nuclear Scattering

To evaluate the cross section (65) for nuclear scattering, we have to specify the interaction potential with the nucleus. To derive this interaction potential is one of the fundamental

problems of nuclear physics. Fermi has proposed a phenomenological potential based on the argument that the wave length of thermal neutrons is much larger than the nuclear radius. This means that the nuclei are point-like scatterers and lead to isotropic, Q-independent, (so-called s-wave) scattering. The same argument holds for classical Thomson scattering, where the only angular dependence came from a polarisation factor. We will therefore use the so-called *Fermi-pseudo-potential:*

$$V\left(\underline{r}\right)=\frac{2\pi\hbar^2}{m}b\delta\left(\underline{r}-\underline{R}\right) \tag{66}$$

to evaluate the cross section (65).

Note, that despite the fact that the strong interaction of high energy physics is responsible for the scattering of the neutron with the nucleus, the scattering probability is small due to the small nuclear radius. Therefore, we can apply the first Born approximation. The quantity b introduced in (66) is a phenomenological quantity describing the strength of the interaction potential and is referred to as the scattering length. The total cross section of a given nucleus is $\sigma=4\pi\left|b\right|^2$, corresponding to the surface area of a sphere with radius b. Since the interaction potential obviously depends on the details of the nuclear structure, b is different for different isotopes of the given element and also for different nuclear spin states. This fact gives rise to the appearance of so-called *coherent* and *incoherent scattering.*

When calculating the scattering cross section, we have to take into account that the different isotopes are distributed randomly over all sides. Also the nuclear spin orientation is random except for very low temperatures in external magnetic fields. Therefore we have to average over the random distribution of the scattering length in the sample:

$$\begin{aligned}\frac{d\sigma}{d\Omega}&=\left\langle\sum_i b_i\, e^{i\underline{Q}\cdot\underline{r}_i}\sum_j b_j^*\, e^{-i\underline{Q}\cdot\underline{r}_j}\right\rangle=\sum_i\sum_j\left\langle b_i b_j^*\right\rangle e^{i\underline{Q}\left(\underline{r}_i-\underline{r}_j\right)}\\&=\left\langle b\right\rangle^2\left|\sum_i e^{i\underline{Q}\cdot\underline{r}_i}\right|^2+N\left\langle\left(b-\left\langle b\right\rangle\right)^2\right\rangle\end{aligned} \tag{67}$$

The scattering cross section is the sum of two terms. Only the first term contains the phase factors $e^{i\underline{Q}\underline{r}}$, which result from the coherent superposition of the scattering from pairs of scatterers. This term takes into account interference effects and is therefore named *coherent scattering*. Only the scattering length averaged over the isotope and nuclear spin distribution enters this term. The second term in (67) does not contain any phase information and is proportional to the number N of atoms (and not to $N^2$!). This term is not due to the interference of scattering from different atoms. It corresponds to scattering from single atoms proportional to the mean square deviation from the average scattering length, which subsequently super impose in an incoherent manner (adding intensities, not amplitudes!). For this reason, the intensity is proportional to the number N of atoms. Therefore, the second term is called *incoherent scattering*. Incoherent scattering gives rise to an isotropic background.

In summary for each element we can define a coherent and an incoherent scattering cross section by the following equations:

$$\sigma_{coh} = 4\pi \langle b \rangle^2 \tag{68}$$

$$\sigma_{inc} = 4\pi \left\langle \left( b - \langle b \rangle \right)^2 \right\rangle \tag{69}$$

The most prominent example for isotope incoherence is elementary nickel. The scattering lengths of the nickel isotopes are listed together with their natural abundance in Table 1. The coherent and incoherent scattering cross sections can be calculated according (68) and (69) and are also given in Table 1. The large incoherent cross section of nickel is mainly due to isotope incoherence.

| Isotope | Natural Abundance | Nuclear Spin | Scattering Length [fm] |
|---|---|---|---|
| $^{58}$Ni | 68.27 % | 0 | 14.4(1) |
| $^{60}$Ni | 26.10 % | 0 | 2.8(1) |
| $^{61}$Ni | 1.13 % | $^3/_2$ | 7.60(6) |
| $^{62}$Ni | 3.59 % | 0 | -8.7(2) |
| $^{64}$Ni | 0.91 % | 0 | -0.37(7) |
| Ni | | | 10.3(1) |
| $\Rightarrow {}_{28}\mathrm{Ni}: \ \sigma_{coh} = 13.3 \text{ barn}; \sigma_{inc} = 5.2 \text{ barn}$ | | | |

**Table 1** *Scattering lengths for the nickel isotopes and resulting cross sections for natural Ni.*

The most prominent example for nuclear spin incoherent scattering is elementary hydrogen. The nucleus of the hydrogen atom - the proton - has the nuclear spin I = 1/2. The total nuclear spin of the system H + n can therefore adopt two values: J = 0 and J = 1. Each state has its own scattering length: $b_- = -47.5$ fm for the singlet state (J = 0) and $b_+ = 10.85$ fm for the triplet state (J = 1). With the relative weight 1/4 and 3/4 for the singlet and triplet state, respectively, the cross sections can be calculated according to (68) and (69) to be:

$$\Rightarrow {}_1H: \ \sigma_{coh} = 1.76 \, barn; \ \sigma_{inc} = 80.26 \, barn \tag{70}$$

(70) shows that hydrogen scatters mainly incoherently. As a result, we observe a large background for all samples containing hydrogen. Finally, we note that deuterium with nuclear spin I = 1 has a much more favourable ratio between coherent and incoherent scattering:

$$\sigma^D_{coh.} = 5.592(7) barn; \quad \sigma^D_{inc.} = 2.05(3) barn \tag{71}$$

The coherent scattering lengths of hydrogen (-3.74 fm) and deuterium (6.67 fm) are significantly different. This can be used for contrast variation by isotope substitution in all samples

containing hydrogen, i. e. in biological samples or soft condensed matter samples, see corresponding lectures.

## 3.5 Magnetic Neutron Scattering

So far, we have only discussed the scattering of neutrons by the atomic nuclei. Apart from nuclear scattering, the next important process is the scattering of neutrons by the magnetic moments of unpaired electrons. This so-called magnetic neutron scattering comes about by the magnetic dipole-dipole interaction between the magnetic dipole moment of the neutron and the magnetic field of the unpaired electrons, which has spin and orbital angular momentum contributions This magnetic neutron scattering allows us to study the magnetic properties of a sample on an atomic level, i. e. with atomic spatial- and atomic energy- resolution. In what follows, we will give an introduction into the formalism of magnetic neutron scattering, restricting ourselves to the case of elastic magnetic scattering. Inelastic magnetic scattering will we discussed in subsequent lectures.

To derive the magnetic scattering cross section of thermal neutrons, we consider the situation shown in Figure 14: a neutron with the nuclear moment $\mu_N$ is at position $\underline{R}$ with respect to an electron with spin $\underline{S}$, moving with a velocity $\underline{v}_e$.

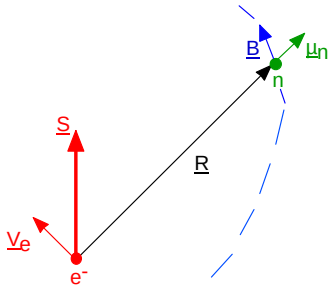


**Figure 14** *Geometry for the derivation of the interaction between neutron and electron.*

Due to its magnetic dipole moment, the neutron interacts with the magnetic field of the electron according to:

$$\mathbf{V}_m = -\underline{\mu}_n \cdot \underline{B} \tag{72}$$

Here, the magnetic moment of the neutron is given by:

$$\underline{\mu}_n = -\gamma_n \mu_N \cdot \underline{\sigma} \tag{73}$$

$\underline{\sigma}$ denotes the spin operator, $\mu_N$ the nuclear magneton and $\gamma_N$ = -1.913 the gyromagnetic factor of the neutron. The magnetic field $\underline{B}$ of an electron is due to a spin- and orbital- part $\underline{B} = \underline{B}_S + \underline{B}_L$. The dipole field of the spin moment is given by:

$$\underline{B}_S = \underline{\nabla} \times \left( \frac{\underline{\mu}_e \times \underline{R}}{R^3} \right) \quad ; \quad \underline{\mu}_e = -2\mu_B \cdot \underline{S} \tag{74}$$

The field due to the movement of the electron is given according to Biot-Savart:

$$\underline{B}_L = \frac{-e}{c} \frac{\underline{v}_e \times \underline{R}}{R^3} \tag{75}$$

The magnetic scattering cross section for a process, where the neutron changes its wave vector from $\underline{k}$ to $\underline{k}'$ and the projection of its spin moment to a quantisation axis z from $\sigma_z$ to $\sigma_z'$ can be expressed within the first Born approximation:

$$\frac{d\sigma}{d\Omega} = \left( \frac{m_n}{2\pi\hbar^2} \right)^2 \left| \left\langle \underline{k}' \sigma_z' \middle| \mathbf{V}_m \middle| \underline{k} \sigma_z \right\rangle \right|^2 \tag{76}$$

As mentioned, we only consider the single differential cross section for elastic scattering. Introducing the interaction potential from (72) to (75) in (76) we obtain after some algebra [4, 15]:

$$\frac{d\sigma}{d\Omega} = \left( \gamma_n r_0 \right)^2 \left| -\frac{1}{2\mu_B} \left\langle \sigma_z' \middle| \underline{\sigma} \cdot \underline{M}_\perp \left( \underline{Q} \right) \middle| \sigma_z \right\rangle \right|^2 \tag{77}$$

The pre-factor $\gamma_n r_0$ has the value $\gamma_n r_0 = 0.539 \cdot 10^{-12}$ cm = 5.39 fm. Here, $\underline{M}_\perp(\underline{Q})$ denotes the component of the Fourier transform of the sample magnetisation, which is perpendicular to the scattering vector $\underline{Q}$:

$$\underline{M}_\perp \left( \underline{Q} \right) = \hat{\underline{Q}} \times \underline{M} \left( \underline{Q} \right) \times \hat{\underline{Q}} \tag{78}$$

$$\underline{M} \left( \underline{Q} \right) = \int \underline{M} \left( \underline{r} \right) e^{i \underline{Q} \cdot r} d^3 r \tag{79}$$

The total magnetisation is given as a sum of the spin- and orbital-angular- momentum part according to:

$$\underline{M}(\underline{r}) = \underline{M}_S(\underline{r}) + \underline{M}_L(\underline{r})$$
$$\underline{M}_S(\underline{r}) = -2\mu_B \cdot \underline{S}(\underline{r}) = -2\mu_B \sum_i \delta(\underline{r} - \underline{r}_i)\underline{S}_i \qquad (80)$$

(77) tells us that with magnetic neutron scattering, we are able to determine the magnetisation $\underline{M}(\underline{r})$ in microscopic atomic spatial co-ordinates $\underline{r}$. This gives a lot more information than a simple macroscopic measurement, where we obtain the ensemble average of the magnetisation over the entire sample. We also see from (77) that the orientation of the nuclear spin momentum of the neutron (represented by $\sigma_z$) plays an important role in magnetic scattering. This is not surprising, since magnetism is a vector property of the sample and obviously there should be an interaction with the vector property of the neutron, its nuclear magnetic moment. Therefore, the analysis of the change of the direction of the neutron nuclear moment in the scattering process should give us valuable additional information as compared to a determination of the change of energy and momentum direction of the neutron alone. These so-called polarisation analysis experiments are discussed in the following lecture. Finally, to obtain an idea of the size of magnetic scattering relative to nuclear scattering, we can replace the matrix element in (77) for a spin ½ particle by the value 1 $\mu_B$. This gives us an "equivalent" scattering length for magnetic scattering of 2.696 fm for a spin ½ particle. This value corresponds quite well to the scattering length of cobalt, which means that magnetic scattering is comparable in magnitude to nuclear scattering.

In contrast to nuclear scattering, we obtain for magnetic scattering a directional term: neutrons only "see" the component of the magnetisation perpendicular to the scattering vector (see Figure 15).

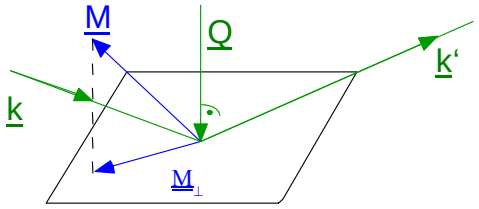


**Figure 15** *For magnetic neutron scattering, only the component $\underline{M}_\perp$ of the magnetisation perpendicular to the scattering vector $\underline{Q}$ is of relevance.*

A second speciality of magnetic scattering as compared to nuclear scattering is the existence of the *magnetic form factor*. How the form factor comes about is most easily understood in the simple case of pure spin scattering, i. e. for atoms with spherical symmetric (L = 0) ground state, such as $Mn^{2+}$ or $Fe^{3+}$. Moreover, the derivation is simplified for ionic crystals, where the electrons are located around an atom. We denote the spin operators of the electrons of atom i with $\underline{s}_{ik}$. The spatial co-ordinates of the electron number k in atom i are $\underline{r}_{ik} = \underline{R}_i + \underline{t}_{ik}$, where $\underline{R}_i$ denotes the position vector to the nucleus of atom i. Now we proceed to separate the intra-atomic quantities. We can write the operator for the magnetisation density as:

$$\underline{M}_S(\underline{r}) = -2\mu_B \sum_{ik} \delta(\underline{r} - \underline{r}_{ik}) \cdot \underline{s}_{ik} \tag{81}$$

The Fourier transform of this magnetisation density is calculated to:

$$\underline{M}(\underline{Q}) = \int \underline{M}_S(\underline{r}) e^{i\underline{Q}\cdot r} d^3r = \sum_{ik} e^{i\underline{Q}\cdot r_{ik}} \underline{s}_{ik} = \sum_i e^{i\underline{Q}\cdot \underline{R}_i} \sum_k e^{i\underline{Q}\cdot t_{ik}} \cdot \underline{s}_{ik} \tag{82}$$

To calculate the scattering cross section, we now have to determine the expectation value of this operator for the quantum mechanical state of the sample averaged over the thermodynamic ensemble. This leads to

$$\underline{M}(\underline{Q}) = -2\mu_B \cdot f_m(\underline{Q}) \cdot \sum_i e^{i\underline{Q}\cdot \underline{R}_i} \cdot \underline{S}_i \tag{83}$$

The single differential cross section for elastic scattering is thus given by:

$$\frac{d\sigma}{d\Omega} = (\gamma_n r_0)^2 \left| f_m(\underline{Q}) \sum_i S_{i\perp} e^{i\underline{Q}\underline{R}_i} \right|^2 \tag{84}$$

Here, $f_m(\underline{Q})$ denotes the form factor, which is connected with the spin density of the atom via a Fourier transform:

$$f_m(\underline{Q}) = \int_{Atom} \rho_s(\underline{r}) e^{i\underline{Q}\cdot r} d^3r \tag{85}$$

With the form (84), we have expressed the cross section in simple atomic quantities, such as the expectation values of the spin moment $\underline{S}_i$ at the various atoms. The distribution of the spin density within an atom is reflected in the magnetic form factor (85).

For ions with spin and orbital angular momentum, the cross section takes a significantly more complicated form [4]. Under the assumption that spin- and orbital- angular momentum of each atom couple to the total angular momentum $\underline{J}_i$ (L/S-coupling) and for rather small momentum transfers (the reciprocal magnitude of the scattering vector has to be small compared to the size of the electron orbits), we can give a simple expression for this cross section in the so-called *dipole approximation*:

$$\frac{d\sigma}{d\Omega} = (\gamma_n r_o)^2 \cdot \left| \frac{g_J}{2} f_m(Q) \sum_i J_{i\perp} e^{i\underline{Q}\cdot\underline{R}_i} \right|^2 \tag{86}$$

Here the magnetic form factor writes:

$$f_m(Q) = \langle j_o(Q) \rangle + C_2 \langle j_2(Q) \rangle \tag{87}$$

$g_J$ denotes the Lande g-factor, $C_2 = \frac{2}{g_J} - 1$ and

$$\langle j_l(Q) \rangle = 4\pi \int_0^\infty j_l(Qr) R^2(r) r^2 dr \tag{88}$$

are the spherical transforms of the radial density distributions R(r) with the spherical Bessel functions $j_l(Qr)$. For isolated atoms, the radial part R(r) has been determined by Hartree-Fock-calculations and the functions $\langle j_0(Q) \rangle$ and $\langle j_2(Q) \rangle$ in (87) have been tabulated [18].

Since the distribution of the magnetic field for spin and orbital angular momentum is completely different, different Q-dependencies of the corresponding form factors result. Moreover, because only the outer electrons in open shells contribute to magnetic scattering, the magnetic form factor also differs from the x-ray form factor introduced above, see Figure 16.

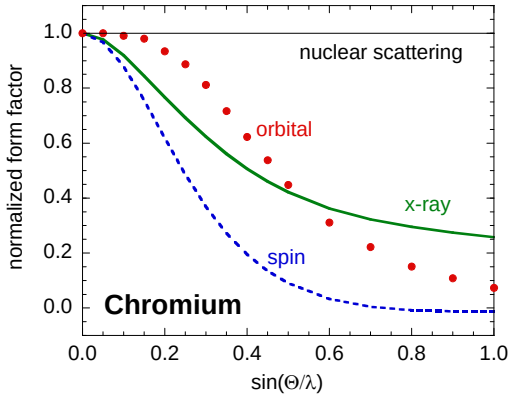


**Figure 16** *Form-factor of Cr [16,17]. Due to the different distribution of the magnetic field for S and L, a more rapid decrease of the scattering amplitude as a function of momentum transfer results for the spin momentum. For the x-ray form factor, the inner electrons play an important role, too. Therefore, the x-ray form factor drops slower as compared to the magnetic form factor. On the Å length scale of the thermal neutron wave length, the nucleus is point-like. Therefore, nuclear scattering is independent of the momentum transfer. Finally, we want to mention that the magnetic form factor can in general be anisotropic, if the magnetisation density distribution is anisotropic.*

## 3.6 Comparison of Probes

Figure 17 shows a double logarithmic plot of the dispersion relation "wave length versus energy" for the three probes neutrons, electrons and photons (compare (45) and (64)). The plot demonstrates, how thermal neutrons of energy 25 meV are ideally suited to determine interatomic distances in the order of 0.1 nm, while the energy of x-rays or electrons for this wavelength is much higher. However with modern techniques at a synchrotron radiation source, energy resolutions in the meV-region become accessible even for photons of around 10 keV corresponding to a relative energy resolution $\Delta E/E \approx 10^{-7}$! The graph also shows that colloids with a typical size of 100 nm are well suited for the investigation with light of energy around 2 eV. These length scales can, however, also be reached with thermal neutron scattering in the small angle region. While Figure 17 thus demonstrates for which energy-wave-length combination a certain probe is particularly useful, modern experimental techniques extend the range of application by several orders of magnitude.

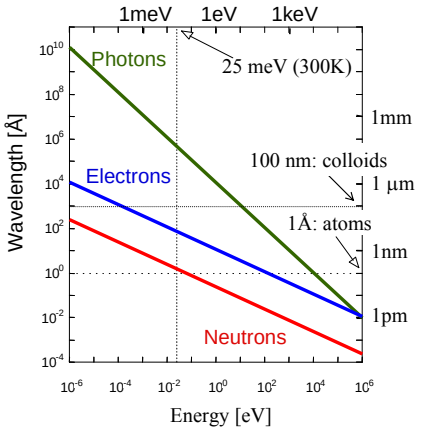


**Figure 17** *Comparison of the three probes - neutrons, electrons and photons - in a double logarithmic energy-wave length diagram.*

It is therefore useful to compare the scattering cross sections as it is done in Figure 18 for x-rays and neutrons. Note that the x-ray scattering cross sections are in general a factor of 10 larger as compared to the neutron scattering cross sections. This means that the signal for x-ray scattering is stronger for the same incident flux and sample size, but that caution has to be applied that the conditions for kinematical scattering are fulfilled. For x-rays, the cross section depends on the number of electrons and thus varies in a monotonic fashion throughout the periodic table. Clearly it will be difficult to determine hydrogen positions with x-rays in the presence of heavy elements such as metal ions. Moreover, there is a very weak contrast between neighbouring elements as can be seen from the transition metals Mn, Fe and Ni in Figure 18. However, this contrast can be enhanced by anomalous scattering, if the photon energy is tuned close to the absorption edge of an element. Moreover, anomalous scattering is sensitive to the anisotropy of the local environment of an atom. For neutrons the cross section depends on the details of the nuclear structure and thus varies in a non-systematic fashion throughout the periodic table. As an example, there is a very high contrast between Mn and Fe. With neutrons, the hydrogen atom is clearly visible even in the presence of such heavy elements as uranium. Moreover there is a strong contrast between the two hydrogen isotopes H and D. This fact can be exploited for soft condensed matter investigations by selectively

deuterating certain molecules or functional groups and thus varying the contrast within the sample.

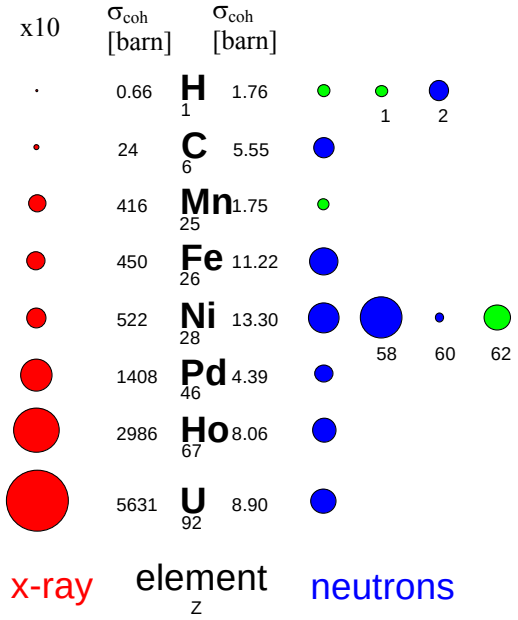


**Figure 18** *Comparison of the coherent scattering cross-sections for x-rays and neutrons for a selection of elements. The area of the coloured circles represent the scattering cross section, where in the case of x-rays a scale factor 10 has to be applied. For neutrons, the green and blue coloured circles distinguish the cases where the scattering occurs with or without a phase shift of π.*

Finally, both neutrons and x-rays allow the investigation of magnetism on an atomic scale. Magnetic neutron scattering is comparable in strength to nuclear scattering, while non-resonant magnetic x-ray scattering is smaller than charge scattering by several orders of magnitude. Despite the small cross sections, non-resonant magnetic x-ray Bragg scattering from good quality single crystals yields good intensities with the brilliant beams at modern synchrotron radiation sources. While neutrons are scattered from the magnetic induction within the sample, x-rays are scattered differently from spin and orbital momentum and thus allow one to measure both form factors separately. Inelastic magnetic scattering e.g. from magnons or so called quasielastic magnetic scattering from fluctuations in disordered magnetic systems is a clear domain of neutron scattering and cannot be done with x-rays up to now. Finally, resonance exchange scattering XRES allows one not only to get enhanced intensities, but also to study magnetism with element- and band sensitivity.

With appropriate scattering methods, employing neutrons, x-rays or light, processes in condensed matter on very different time and space scales can be investigated. Which scattering method is appropriate for which region within the "scattering vector Q - energy E plane" is plotted schematically in Figure 19. A scattering vector Q corresponds to a certain length scale, an energy to a certain frequency, so that the characteristic lengths and times scales for the various methods can be directly determined from the Figure. More information on the instrumentation was given in earlier lectures. Examples for applications will follow in subsequent lectures.

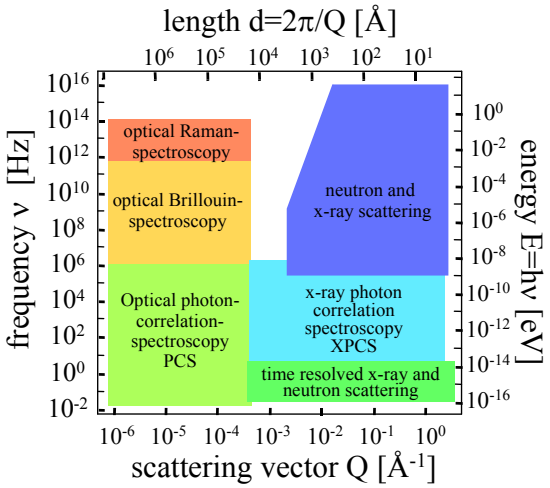


**Figure 19** *Regions in frequency ν and scattering vector Q or energy E and length d plane, which can be covered by various scattering methods.*

# 4 Examples for Structure Determination

After having introduced the basic concepts and cross sections, we will concentrate in the remaining part of this lecture on purely elastic scattering and discuss two examples for structure determinations employing either neutrons or x-rays. The first example deals with the determination of chemical and magnetic structure of a colossal magnetoresistance CMR manganite $La_{1-x}Sr_xMnO_3$ from neutron powder diffraction data. The second example demonstrates, which element- and band specific information we can obtain from XRES in the case of a multiferroic material $TbMnO_3$. These examples were chosen, because both materials belong to the class of highly correlated electron systems. Materials with strong electronic correlations present a real challenge to modern condensed matter physics, as they show a wealth of phenomena which cannot be explained within the "standard model" of solid state physics, such as unusual superconductivity, metal-insulator transitions, huge magnetocaloric effects, colossal magnetoresistance (i.e. a strong dependence of the electrical resistivity on the external magnetic field) and multiferroic behaviour (e.g. simultaneous magnetic and ferroelectric long range order). These novel functionalities make correlated electron systems prime candidates for applications, e.g. in information storage. A characteristic feature is that the ground states are determined by a delicate balance of several interacting degrees of freedom. In order to reach a deeper understanding of these materials, the order and excitations of spin-, charge-, orbital- and lattice degrees of freedom have to be determined, which is a typical task for scattering methods. In this chapter, we concentrate on the order of spin and lattice, while charge and orbital order, as well as the lattice and spin excitations will be discussed in subsequent lectures.

## 4.1 Neutron Powder Diffraction from a CMR Manganite

Figure 20 shows a proposed phase diagram of $La_{1-x}Sr_xMnO_3$ manganites. The phase diagram is extremely rich. Small changes in external parameters (here temperature or chemical potential) lead to huge changes in the order and physical properties, since the delicate balance

between the different degrees of freedom is shifted. Of particular interest are compositions close to x = 1/8, where a double transition from a paramagnetic insulating phase to a ferromagnetic metallic phase and then to a ferromagnetic insulating phase occurs with decreasing temperature. It has been shown with resonant x-ray scattering from a single crystal that this double transition is connected with changes in the charge- and orbital order, see corresponding lecture. Here we concentrate on the lattice and magnetic order of these compounds. The order of the lattice can be studied most efficiently combining x-ray and neutron powder diffraction, while the study of magnetic order is a domain of neutron powder diffraction.

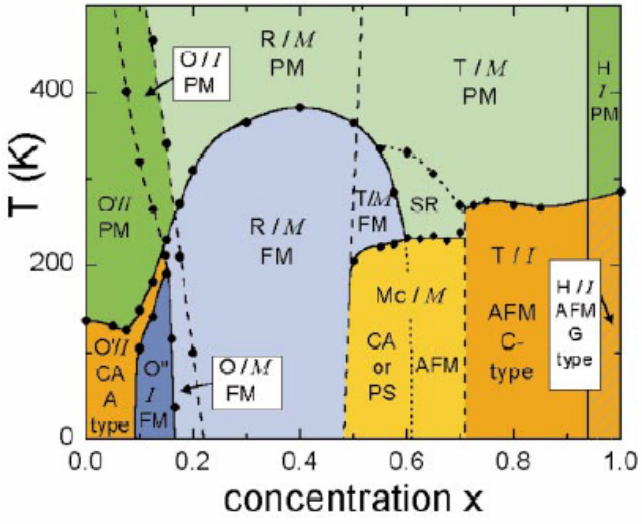


**Figure 20** *Proposed phase diagram for $La_{1-x}Sr_xMnO_3$ manganites according to [19]. R, O, T, H label the crystallographic phases Rhombohedral, Orthorhombic, Tetragonal and Hexagonal. M stands for Metal, I for Insulator. Magnetic order is indicated by PM, FM, AFM, CA or PS for Paramagnetic, Ferromagnetic, Antiferromagnetic, Canted or Phase separated, respectively.*

Due to the extreme sensitivity on external parameters, small changes in the stoichiometry of these compounds lead to huge effects in the physical parameters. This might be the reason for different structures, transition temperatures etc reported in the literature. In [20], we report a detailed study of nominal $La_{1-x}Sr_xMnO_3$ prepared under different conditions. A powder sample was prepared from solid state reactions. Part of the sample has been annealed in Ar atmosphere, another part in $O_2$ atmosphere. A huge effect is observed in the magnetic properties, see Figure 21. The Curie temperature is reduced for the Ar annealed sample by about 20 %.

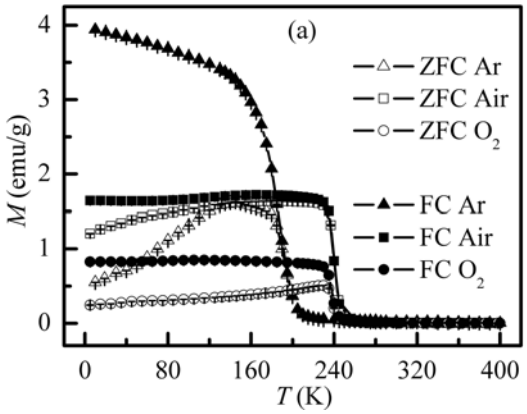


**Figure 21** *Zero field cooled ZFC and field cooled FC magnetization M vs. temperature measured at H = 20 Oe for three $La_{0.875}Sr_{0.125}Mn_{1-\gamma}O_{3+\delta}$ samples prepared in air, annealed in Ar or $O_2$ atmosphere [20].*

In order to correlate this drastic effect with structural features, we have performed a combined x-ray and neutron powder diffraction study. The two probes have different contrast ratios for the different elements. Using the information from both probes, the relative content of the various elements can be determined with higher precision as compared to one probe alone. To overcome the problem of overlapping Bragg peaks, a profile refinement method is chosen. In this method, the peak position and intensity is calculated for each Bragg reflection and a profile function, which takes into account the instrumental resolution, is assigned to each peak [21]. Figure 22 shows the result of such a refinement.

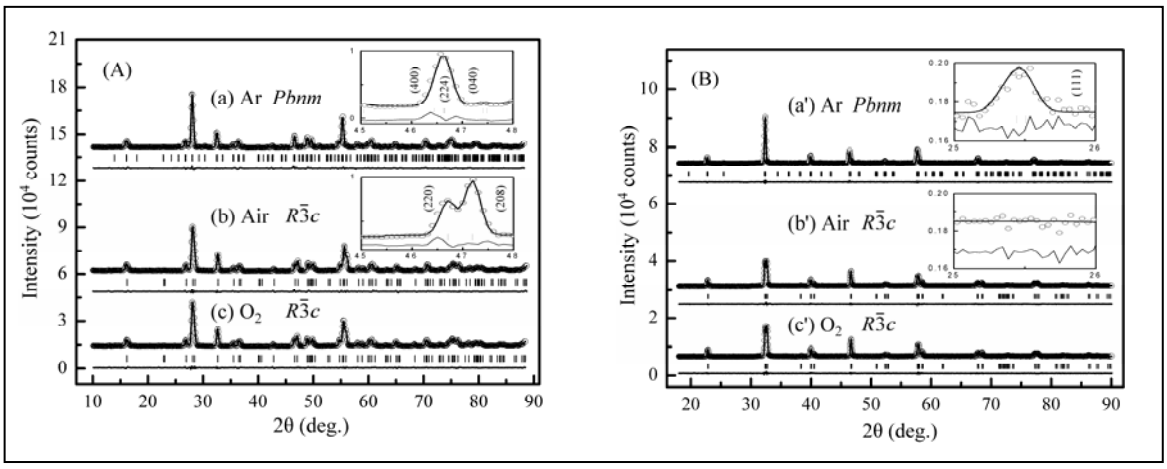


**Figure 22** *Observed (circles) and calculated (solid lines) patterns of neutron (A) and x-ray (B) powder diffraction diagrams for the Ar annealed (a) and (a'), air sintered (b) and (b') and oxygen annealed (c) and (c') $La_{0.875}Sr_{0.125}Mn_{1-\gamma}O_{3+\delta}$ samples at ambient conditions. The bars mark the positions of Bragg reflections automatically generated from the space group. The lower curves in each panel represent the difference between the observed and calculated patterns. The insets show magnified patterns in certain 2θ regions [20].*

The site occupancies of the different elements could be determined with high precision. For the Ar annealed sample, we observe a decrease of the O site occupancy by 2.2 %. This decrease leads to a structural change from rhombohedral to orthorhombic and to a decrease of the Curie temperature by about 20 %! The latter effect can be explained from the structural data by a decrease of the total strength of the magnetic interactions due to a change in the Mn-O-Mn bond angle and a decrease of the numbers of nearest neighbours.

Finally, we show in Figure 23 the result of a neutron powder refinement of the chemical and magnetic structure of a powdered single crystal sample for x = 1/8 for T = 5K. Ferromagnetic order is seen by an additional intensity on top of structural Bragg peaks, while additional superstructure reflections arise from the larger unit cell of antiferromagnetic order. The structural information obtained from neutron powder diffraction provides the basis for establishing the correct charge- and orbital- order model from single crystal anomalous x-ray scattering.

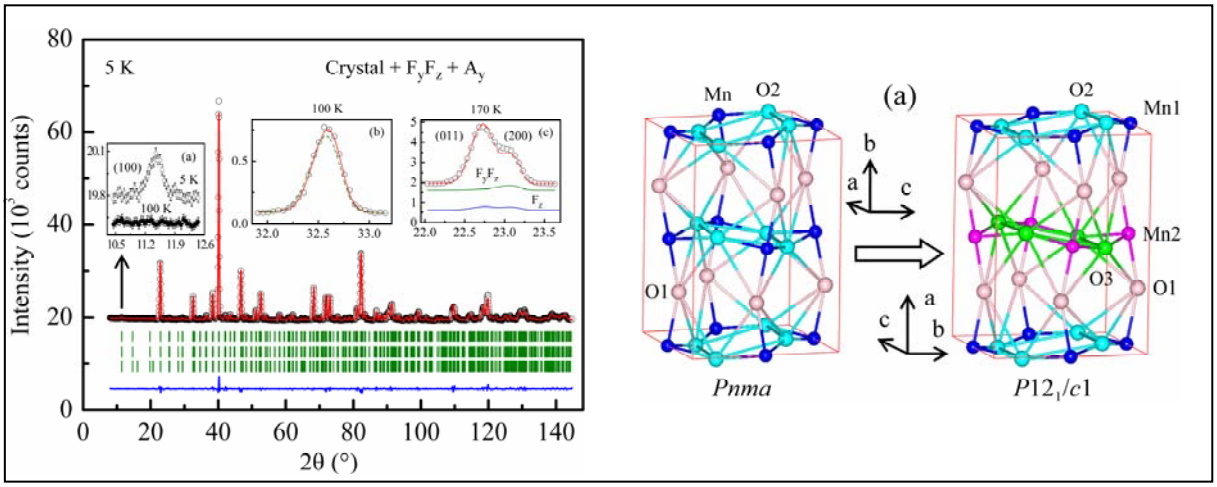


**Figure 23** *Left: Rietveld refinement plot of the NPD data of a $La_{1-x}Sr_xMnO_3$ ($x \approx 1/8$) powdered single crystal in $P12_1/c1$ symmetry at 5 K. The contributions to the calculated intensity (solid line) are from the crystal, ferromagnetic (FM) ($F_yF_z$) and A-type antiferromagnetic (A-AFM) ($A_y$) structures. $F_y$, $F_z$ and $A_y$ denote the FM moments along the b and c axes and the A-AFM moment along the b axis, respectively. Inset (a) shows the appearance of an A-AFM peak (100) at 5 K. Insets (b) and (c) compare the quality of the refinements with different FM models $F_yF_z$ and $F_z$. Right: Schematic illustrations of the unit cells of the crystal structure for the orthorhombic (Pnma) and monoclinic ($P12_1/c1$) models.*

## 4.2 Resonance Exchange Scattering from a Multiferroic Material

The observation of the multiferroic effect in a variety of manganites containing small Rare Earth cations [22] has triggered renewed interest in the magneto-electric effect [23]. In these compounds exists a strong coupling between the ferroelectric polarization and an (anti)ferromagnectic order of the spin system. From the theoretical point of view these compounds challenge the standard explanation for ferroelectricity and magnetic order in transition metal systems. The former usually requires the *d*-notness, i.e. empty *d* orbitals, while the latter can only appear, if partly filled 3*d* orbitals are present. From the applied point of view the control of electrical degrees of freedom via magnetic fields and vice versa offers

fascinating new perspectives, e.g. devices, where a magnetic field changes the optical properties.

$TbMnO_3$ crystallizes in the Perowskite structure, space group *Pbnm*. The magnetic structure of $TbMnO_3$ has been studied by single crystal neutron diffraction, e.g. [24]. At the Néel-Temperature $T_N \approx 41$ K, an incommensurate magnetic structure appears (i.e. the magnetic and lattice periods are not just in a simple rational ratio), with a mainly sinusoidal modulation. According to the neutron diffraction results, only the Mn moments order and are aligned along the b direction. At the ferroelectric transition temperature $T_C$ ($\approx 25$ K in our case), the magnetic structure of the Mn ions becomes spiral, with the ordered moments mainly in the b-c plane. In addition, neutron diffraction suggests the existence of a small *a*-axis component of the $Tb^{3+}$ ions. Below about 8 K the moments of the Tb subsystem order with a different propagation vector. There are suggestions that the broken inversion symmetry due to the non-collinear magnetic structure is necessary to explain the ferroelectric polarization along the *c* direction for $T<T_C$.

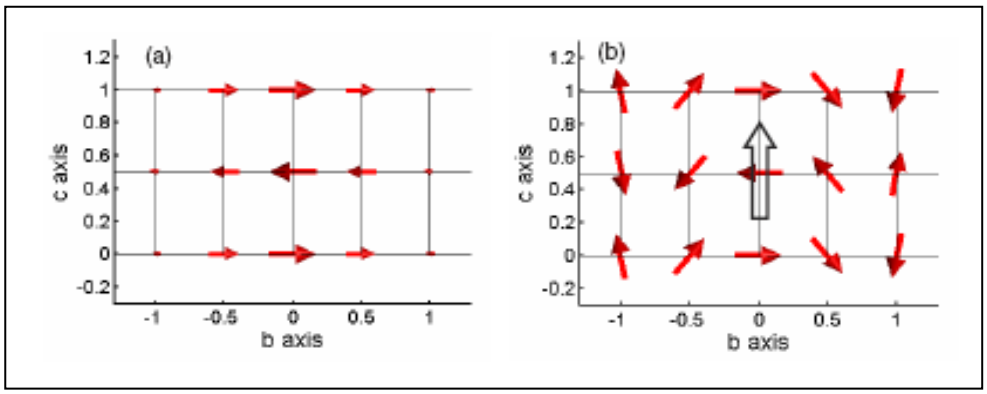


**Figure 24** *Magnetic structure of the Mn subsystem of $TbMnO_3$ at temperatures above (left, a) and below (right, b) the ferroelectric ordering temperature $T_C \approx 25$K according to [24].*

Which additional information can be obtained from x-ray scattering? While in neutron diffraction, the magnetism of Mn and Tb can only be disentangled using models for the magnetic structures, resonance exchange scattering XRES gives us direct access to the magnetic order of the various subsystems. Moreover, for incommensurate structures, a more precise determination of the magnetic propagation vector is possible due to the better reciprocal space resolution of synchrotron x-ray radiation.

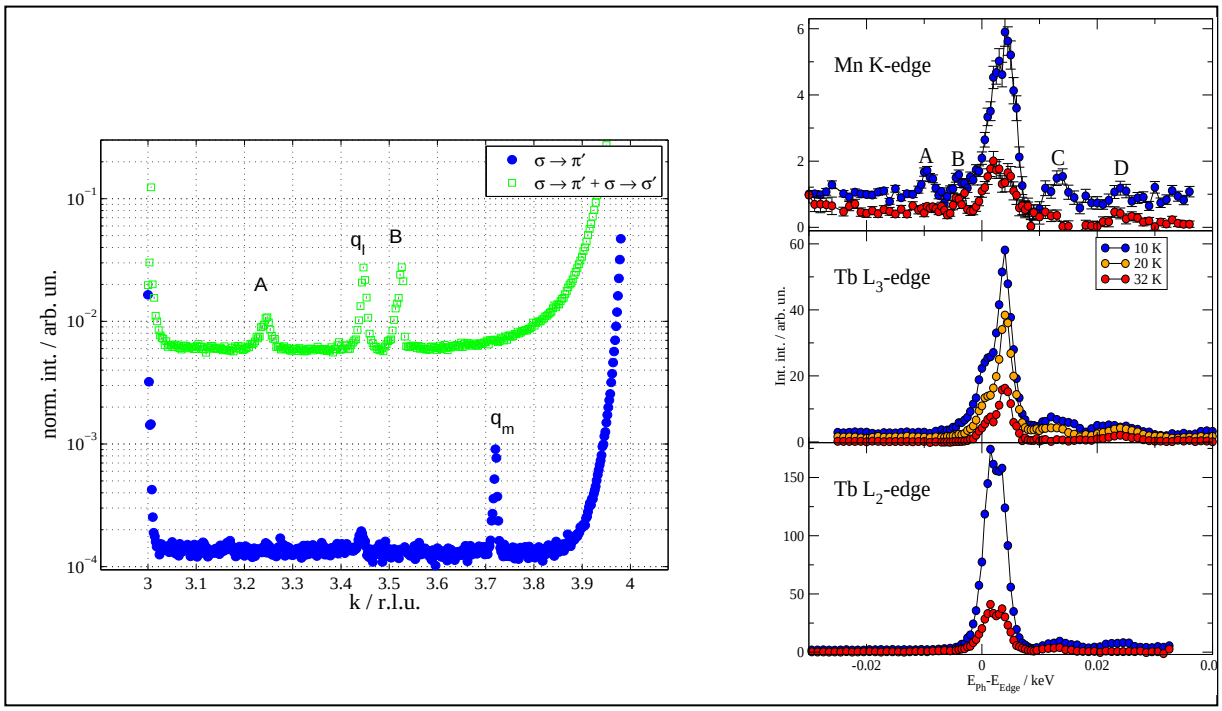


**Figure 25** *Left: Linear scans in reciprocal space. The data plotted in green was taken off resonance and without polarization analysis. While the peaks denoted with A and B are background features, the peak marked with $q_l$ indicates a structural distortion. The data in blue was taken at the Tb $L_{III}$ resonance for the $\sigma \rightarrow \pi'$ polarization channel. The peak marked with $q_m$ is of magnetic origin. Right: Enhancement of XRES from $TbMnO_3$ at different temperatures for the various absorption edges according to [25].*

In Figure 25 we show the resonance enhancement at the Mn K and Tb $L_{II}$ and $L_{III}$ edges [25]. If the x-ray energy is tuned to the maximum of the resonance at the Tb $L_{II}$ edge, an enhancement of more than two orders of magnitude occurs relative to non-resonant scattering, so that effectively we only observe the scattering from the Tb subsystem. It came as a big surprise that we observe scattering from the Tb subsystem also above the ferroelectric transition temperature $T_C$, where neutron scattering suggests that the Tb subsystem is completely disordered. In Fig. 26 we plot the full temperature dependence for the magnetic propagation vector and for the integrated intensities. It can be seen that a "quasi-" lock-in transition occurs at $T_C$, i.e. the temperature dependence becomes weak but does not vanish below this temperature. The integrated intensities can be well described with a model assuming an order of the Mn moments and an associated induced moment in the Tb 5d band above $T_C$. Below $T_C$, the Tb 4f moments order in addition [25]. Please note that for dipolar transitions, XRES at the rare earth L edges is sensitive to the exchange splitting of the 5d states, and not directly to the magnetism of the 4f electrons, while neutrons see mainly the latter. Therefore the XRES study reveals a very intimate coupling of the spin polarization of Mn and of the Tb 5d states. Such a coupling is rather unusual for an insulator like $TbMnO_3$ and must be taken into account for any model explaining the multiferroic behaviour.

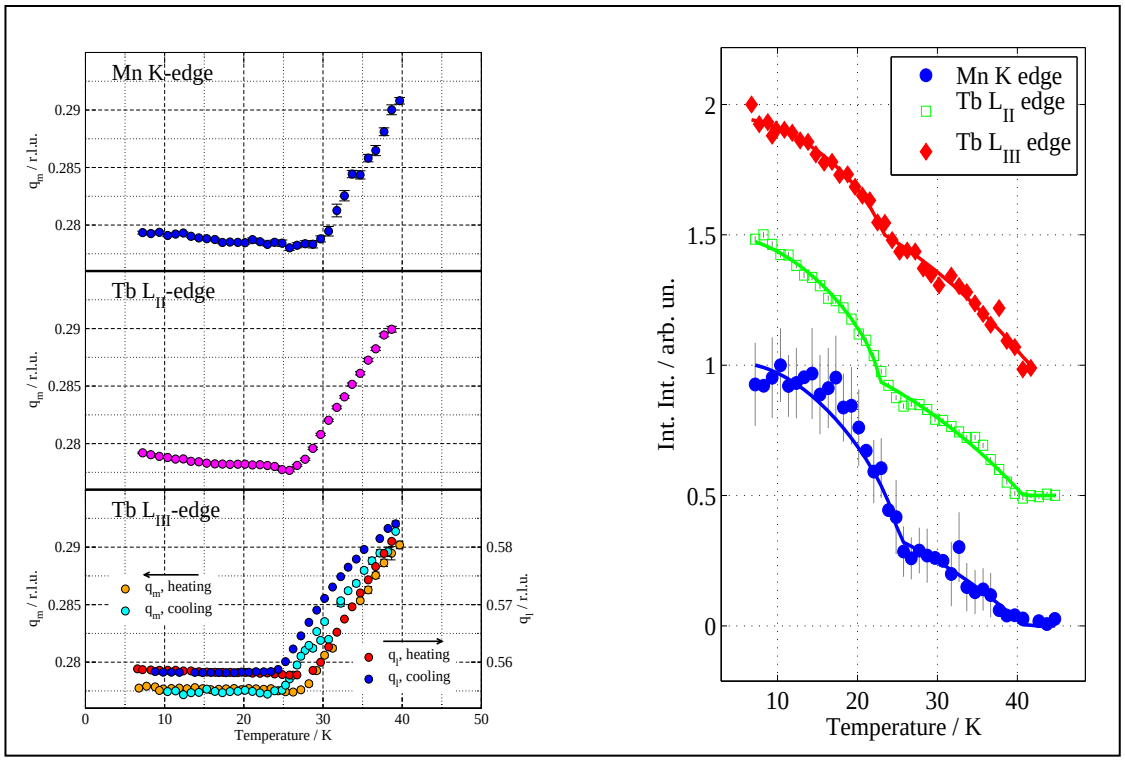


**Figure 26** *Left: Temperature dependence of the magnetic propagation vector and the associated structural distortion according to [25]. Right: Temperature dependence of the integrated intensity of XRES at the various absorption edges together with a refinement according to [25].*

In summary, this example nicely shows how neutron diffraction is a very powerful tool to determine complex magnetic structures and how XRES provides additional element- and band specific information. This detailed information on the magnetic and chemical order is the basis for an explanation of the physical effects – here the multiferroic effect – in any magnetic material.

# References

[1] Th. Brückel, G. Heger, D. Richter and R. Zorn (Eds), "Neutron Scattering",

Schriften des Forschungszentrums Jülich: Materie und Material **28** (2005).

[2] D. Richter, „Scattering Techniques I: Neutron Diffraction“

and Th. Brückel, „Scattering Techniques II: Magnetic X-Ray Scattering“

in S. Blügel, Th. Brückel and C.M. Schneider (Eds), "Magnetism goes Nano",

Schriften des Forschungszentrums Jülich: Materie und Material **26** (2005).

[3] J. M. Cowley, "Diffraction Physics" (North Holland Amsterdam, 1990).

[4] S. W. Lovesey, "Theory of neutron scattering from condensed matter" (Clarendon Press, Oxford, 1987).

[5] B. W. Batterman and H. Cole, Rev. Mod. Phys. **36** (1964) 681.

[6] W. H. Zachariasen, "Theory of X-Ray Diffraction in Crystals", (Dover, New York, 1994).

[7] M. Blume, J. Appl. Phys. **57** (1985) 3615.

[8] M. Blume and D. Gibbs, Phys. Rev. B **37** (1988) 1779.

[9] M. Blume in G. Materlik, C. J. Sparks and K. Fischer (Eds), “Resonant Anomalous X-Ray Scattering”, (North-Holland, Amsterdam, 1994).

[10] S. M. Durbin, Phys. Rev. B **57** (1998) 7595.

[11] F. de Bergevin and M. Brunel, Acta Cryst. A **37** (1981) 314.

[12] J. P. Hannon, G. T. Trammell, M. Blume and D. Gibbs, Phys. Rev. Lett. **61** (1988) 1245 and Erratum: Phys. Rev. Lett. **62** (1989) 2644.

[13] J. P. Hill and D. F. McMorrow, Acta Cryst. A **52** (1996) 236.

[14] Templeton & Templeton, Acta Cryst. A **36** (1980) 436.

[15] M. Blume, Phys. Rev. **130** (1963) 1670.

[16] J. Strempfer, Th. Brückel et al., Eur. Phys. J. B **14** (2000) 63.

[17] J. Strempfer, Th. Brückel et al., Physica B **267-268** (1999) 56.

[18] J. Brown in A.J. Wilson (Ed.), “Int. Tables for X-ray Crystallography C” (Dordrecht : Kluwer Academic Publ., 1999).

[19] J. Hemberger et al., Phys. Rev. B **66** (2002) 094410.

[20] H. F. Li et al., J. Phys.: Condens. Matter **19** (2007) 016003.

[21] J. M. Rietveld, J. Appl. Crystallogr. **2** (1969) 65.

[22] T. Kimura et al., Nature **426** (2003) 55.

[23] M. Fiebig, J. Phys. D: Appl Phys. **38** (2005) R123.

[24] M. Kenzelmann et al., Phys. Rev. Lett. **95** (2005) 087206.

[25] J. Voigt, J. Perßon, J. W. Kim and Th. Brückel; submitted.